Department of Civil Engineering

Nonlocal continuum damage models for quasi-brittle fracture: algorithms and applications

Hoang-Anh-Tuan Nguyen

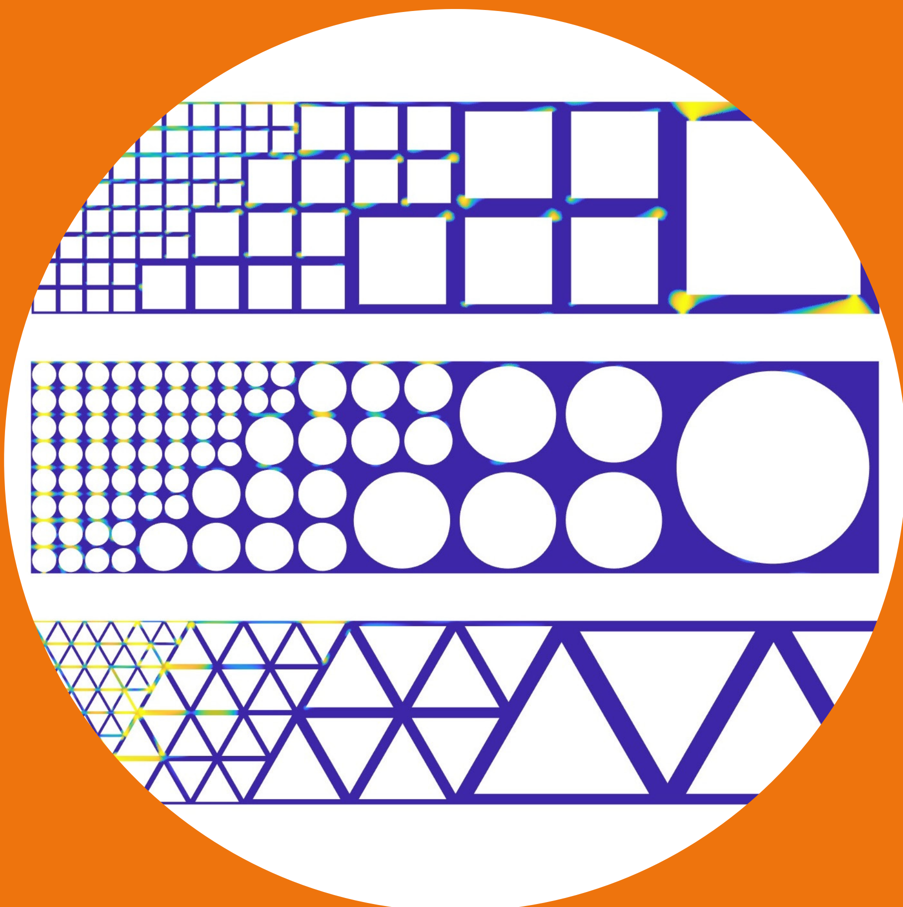

Aalto University

DOCTORAL DISSERTATIONS

Aalto University publication series
DOCTORAL DISSERTATIONS 127/2021

Nonlocal continuum damage models for quasi-brittle fracture: algorithms and applications

Hoang-Anh-Tuan Nguyen

A doctoral dissertation completed for the degree of Doctor of Science (Technology) to be defended, with the permission of the Aalto University School of Engineering, Remote connection link https://aalto.zoom.us/j/7799660770, on 14 October 2021 at 12:00.

Aalto University
School of Engineering
Department of Civil Engineering
Computational Structural Engineering and Mechanics

Supervising professors
Associate Professor Jarkko Niiranen
Department of Civil Engineering, Aalto University, Finland

Thesis advisors
Associate Professor Jarkko Niiranen
Department of Civil Engineering, Aalto University, Finland

Preliminary examiners
Professor Laura De Lorenzis
Department of Mechanical and Process Engineering, ETH Zürich, Switzerland

Professor Anil Misra
Department of Civil, Environmental and Architectural Engineering, The University of Kansas, United States

Opponents
Associate Professor Leong Hien Poh
Department of Civil and Environmental Engineering, National University of Singapore, Singapore

Aalto University publication series
DOCTORAL DISSERTATIONS 127/2021

ISBN 978-952-64-0514-8 (printed)
ISBN 978-952-64-0515-5 (pdf)
ISSN 1799-4934 (printed)
ISSN 1799-4942 (pdf)
http://urn.fi/URN:ISBN:978-952-64-0515-5

Unigrafia Oy
Helsinki 2021

Finland

Printed matter
4041-0619

Aalto University

Aalto University, P.O. Box 11000, FI-00076 Aalto www.aalto.fi

Abstract

Author
Hoang-Anh-Tuan Nguyen

Name of the doctoral dissertation
Nonlocal continuum damage models for quasi-brittle fracture: algorithms and applications

Publisher School of Engineering

Unit Department of Civil Engineering

Series Aalto University publication series DOCTORAL DISSERTATIONS 127/2021

Field of research Civil Engineering

Manuscript submitted 1 June 2021 **Date of the defence** 14 October 2021

Permission for public defence granted (date) 20 August 2021 **Language** English

☐ **Monograph** ☒ **Article dissertation** ☐ **Essay dissertation**

Abstract

Quasi-brittle fracture – characteristic for mineral-based materials typical in construction – concerns a large number of structural failures which, due to the abrupt nature of the phenomenon, may cause loss of lives and damage to infrastructure. Therefore, it is crucial to develop numerical methods, besides certain theoretical and experimental approaches, to predict the whole process of mechanical failure from the elastic phase, the damage initiation, the stable and unstable propagation of failure until the final rupture.

This dissertation studies a continuum damage approach, by focusing on the development of a nonlocal model with enhanced performance and accuracy in the modeling of localized quasi-brittle damage. The damage model is formulated to cope with a wide range of mineral-based materials, including plain and spatially random heterogenous concrete in which the variability of material properties substantially influences the global response of the structures. For the class of microarchitectural materials, the damage model is enriched in light of a simplified form of Mindlin's strain gradient elasticity theory. The gradient-enriched model is proved to be capable of capturing the size effects induced by microarchitectures in both the elastic and the softening regimes, especially in finer scales where the characteristic size of the internal structure is of the same order as the exterior dimensions of the specimen itself.

For thin-walled structures, the damage model is integrated into a plate model of third-order shear deformation theory to remedy the computational burden of the corresponding simulations with nonlinear three-dimensional models. The plate formulations cover various functionally graded material configurations with material properties set to smoothly vary in the direction of the plate thickness.

For the numerical implementations of the dissertation, either the finite element or isogeometric Galerkin methods are employed in the form of an in-house software package. The former, as a de facto industrially accepted methodology for computational mechanics, boasts an excellent capability in meshing complex geometries, whereas the latter is exploited in the present dissertation for the non-standard gradient-enhanced problem settings that require higher-order continuity over element boundaries. Through a series of benchmark problems, the implementations of the numerical methods are verified and the damage models are validated, and the roles of their key features are demonstrated.

Keywords continuum damage, nonlocal interactions, quasi-brittle failure, heterogeneous material, micro-architecture, strain-gradient theory, size effect, third-order shear deformation theory, functionally graded material

ISBN (printed) 978-952-64-0514-8 **ISBN (pdf)** 978-952-64-0515-5

ISSN (printed) 1799-4934 **ISSN (pdf)** 1799-4942

Location of publisher Helsinki **Location of printing** Helsinki **Year** 2021

Pages 196 **urn** http://urn.fi/URN:ISBN:978-952-64-0515-5

Acknowledgments

My doctoral study in the Computational Structural Engineering group at the Department of Civil Engineering, School of Engineering, Aalto University started at the end of 2017 when I got an opportunity to work on an interesting topic on continuum damage modeling. During the study time, I have enjoyed many valuable things such as discussing and collaborating with my friends, colleagues, visiting lecturers, and researchers. I am also benefited from traveling to attend national and international conferences where I have had fruitful discussions with researchers from various backgrounds like physics, mathematics, and practical engineering. These precious experiences cannot be obtained without the generous support and funding from Aalto University, Academy of Finland, and Foundation for Aalto University Science and Technology.

I am deeply grateful to my supervisor and advisor Jarkko Niiranen for allowing me to be his doctoral student and work on this very interesting topic. He has been providing me a lot of guidance concerning the study and supports in my writing, as well as giving me the autonomy to be independent in my research.

I would like to thank all my co-authors for their cooperation in our cooperative works and other colleagues at the Department of Civil Engineering, who warmly help me when I have questions. I am very thankful to Dr. Djebar Baroudi, Dr. Athanasios Markou, and Prof. Reijo Kouhia for fruitful instructions on structural and material mechanics; Loc Tran, Quoc Anh Tran, Daniel Castillo, and Jalal Torabi for informative discussions on numerical methods and material modeling.

My journey in Finland would not be fascinating without friends who are students and researchers from different departments. Together we enjoyed comfortable coffee times, camping, running, and other outdoor activities.

Finally, I would like to address my special appreciation to my parents and sister who always believe in and encourage me to overcome difficulties in all the stages of my life, and my wife Truc Vo for her love, understanding, and great emotional support.

Espoo, 29th April 2021
Hoang-Anh-Tuan Nguyen

Contents

List of Publications

This doctoral dissertation consists of a summary and of the following publications which are referred to in the text by their numerals:

1. Nguyen, Hoang Anh Tuan; Bui, Quoc Tinh; Hirose, Sohichi. 2018. Smoothing gradient damage model with evolving anisotropic nonlocal interaction tailored to low-order finite elements. Elsevier. Computer Methods in Applied Mechanics and Engineering, Volume 328, pages 398-541. ISSN: 0045-7825. https://doi.org/10.1016/j.cma.2017.09.019.

2. Castillo, Daniel; Nguyen, Hoang Anh Tuan; Niiranen, Jarkko. 2021. Spatially random modulus and tensile strength: contribution to variability of strain, damage, and fracture in concrete. SAGE. International Journal of Damage Mechanics. ISSN: 1056-7895. https://doi.org/10.1177/10567895211013081. Available online.

3. Nguyen, Hoang Anh Tuan; Niiranen, Jarkko. 2020. A second strain gradient damage model with an implementation for quasi-brittle materials with microarchitectures. SAGE. Mathematics and Mechanics of Solids, Volume 25, issue 3, pages 515-546. ISSN: 1081-2865. https://doi.org/10.1177/1081286519884695.

4. Nguyen, Hoang Anh Tuan; Niiranen, Jarkko. 2021. Nonlocal continuum damage modeling for functionally graded plates of third-order shear deformation theory. Elsevier. Thin-walled Structures, Volume 164, page 107876. ISSN: 0263-8231. https://doi.org/10.1016/j.tws.2021.107876.

Author’s Contribution

Publication 1: Smoothing gradient damage model with evolving anisotropic nonlocal interaction tailored to low-order finite elements

The author has had the main responsibility for the governing ideas, theoretical formulations, derivations of the numerical discretizations, and accomplishing the numerical simulations, including code development and programming. The main part of writing has been the responsibility of the author as well. Bui has been involved in developing the governing ideas and aided the writing process with edits and comments. Hirose has approved the results and the manuscript.

Publication 2: Spatially random modulus and tensile strength: contribution to variability of strain, damage, and fracture in concrete

The author has taken part in generating the governing idea and accomplished the adaptation of the nonlocal damage model for heterogeneous materials in Section 2, and involved in deriving the simulation results in Section 3, including programming, and essentially contributed to the writing of Section 2 and the Introduction. Castillo has been responsible for the original governing idea and generation of the random fields of materials and taken part in analyzing the results and writing the manuscript. Niiranen has supervised the research and given comments on the text.

Publication 3: A second strain gradient damage model with an implementation for quasi-brittle materials with micro-architectures

The author has had the main responsibility for the governing ideas, theoretical formulations, derivations of the numerical discretizations, and accomplishing the numerical simulations, including code development and programming. The main part of writing has been the responsibility of the author as well. Niiranen has supervised the research, approved the results, and helped by giving comments and suggestions.

Publication 4: Nonlocal continuum damage modeling for functionally graded plates of third-order shear deformation theory

The author has had the main responsibility for the governing ideas, theoretical formulations, derivations of the numerical discretizations, and accomplishing the numerical simulations, including code development and programming. The main part of writing has been the responsibility of the author as well. Niiranen has supervised the research, has been involved in designing the numerical examples, approved the results, and helped by giving comments and suggestions.

1. Introduction

1.1 Background

1.1.1 Overview of fracture and damage modeling

Quasi-brittle fracture, which is the main type of failure in mineral-based materials like rock, concrete, and limestone, causes significant damage to infrastructure systems and loss of lives. Hence, the prediction of failure for this class of material has captivated researchers' attention over the past decades and has been a major branch of computational mechanics, besides theoretical and experimental approaches (see Irwin, 1957; Hillerborg *et al.*, 1976; Nooru-Mohamed, 1992; Koksal and Karakoc, 1999; Kuhl *et al.*, 2000; Aliha *et al.*, 2012; Carpiuc-Prisacari, 2019; and references therein). Some common numerical methods including the finite element method (FEM) (Fish and Belytschko, 2007), isogeometric analysis (IGA) (Hughes *et al.*, 2005; Nguyen *et al.*, 2015), the extended finite element method (XFEM) (Moes *et al.*, 1999; Moes and Belytschko, 2002; Zhang *et al.*, 2015, Salimzadeh and Khalili, 2015). The cohesive zone model (CZM) (Park and Paulino, 2016; Ferte *et al.*, 2016), and the phase-field method (Francfort and Marigo, 1998; Bourdin *et al.*, 2000; Miehe *et al.*, 2010), with different underlying continuum descriptions (Bažant, 1994; Peerlings *et al.*, 2001; Pjaudier-Carbot *et al.*, 2004; Nguyen and Houlsby, 2007; Nguyen, 2011), have been extensively developed to study the fracture problems in materials and structures which are of significant challenges in practice. Besides, plasticity theory has been utilized to describe the inelastic behaviors of concrete (Mikkola and Schnobrich, 1970; Willam and Warnke, 1975; Dragon and Mróz 1979; Menétrey and Willam, 1995; Grassl *et al.*, 2002; Papanikolaou and Kappos, 2007). These models, however, are not capable to represent the gradual degradation of elasticity and the influences of microcracking. To remedy these shortcomings, several researchers have combined damage and plasticity, leading to very complicated models (Ibrahimbegovic *et al.*, 2003; Grassl and Jirásek, 2006; Cicekli *et al.*, Voyiadjis *et al.*, 2008; Jefferson *et al.* 2016). Nevertheless, Mazars and Pjaudier-Carbot (1989, 1996) argued that inelastic behaviors of quasi-brittle materials are much more dependent on damage and microcracking processes than plastic deformations. Therefore, the damage models which do not include plasticity are adequate and have been employed for a majority of real-world problems.

Within the numerical modeling and simulation of localized failure in quasi-brittle materials, the aforementioned methods (without integrating plasticity) can be grouped into two categories as *discrete fracture* and *smeared damage*. The former methods based on linear elastic fracture mechanics theory (LEFM) with the concept of Griffith's energy release rate, *e.g*., XFEM and CZM represent the discontinuities of the crack geometries by embedding an additional field to the approximated primary variable (*i.e*., displacement field). Discrete methods are highly effective when tracking the macrocrack propagation and generating accurate results of the displacement in the cracked domain. Nonetheless, as they require the cracks to be initialized a priori and ad hoc criteria to track the evolution of cracks, which are not trivial in practice, discrete approaches become less efficient when dealing with problems of multiple cracks. Phase-field methods, which are constructed based on LEFM and the energy minimization concept, regularize the discontinuities by a continuous coupling field variable by considering a length scale parameter. The discontinuous crack geometries are diffused through thin bands of a phase-field variable. In turn, the coupling phase field is set to propagate along the paths of least energy. Continuum damage models, while being similar to phase-field methods in terms of mathematical structure, are developed based on the theory of damage mechanics (de Borst and Verhoosel, 2016). The smear damage approaches are appropriate to describe quasi-brittle fracture (Resende, 1987; Bažant and Pjaudier-Carbot, 1989), which exhibits a long softening phase post-peak and eventually leads to failure. In conventional local damage models, when the finite element mesh is refined to a certain level, the irreversible damage over-localizes in a very narrow zone consisting of a few elements. As a result, dissipated energy unphysically vanishes when the element size tends to zero (Jirásek, 2008). In such a case, the numerical solution heavily depends on the mesh size in the damaged area; hence, the local damage models require certain calibrations, *e.g*. adapting the material softening rate concerning element sizes (Rizzi, 1994; Rizzi *et al*., 1995; Kurumatani *et al*., 2016; Alfarah *et al*., 2017; Tran *et al*., 2019), to be utilized in practice. To alleviate these difficulties, a regularization method is adopted in the family of nonlocal damage models (Bažant, 1994; Peerlings *et al*., 1996; Giry *et al*., 2011; Jirásek, 2017, Bui *et al*., 2017). Specifically, in strain-driven damage approaches (Peerlings *et al*., 2004; Poh and Sun, 2017; Nguyen *et al*., 2018), the nonlocal equivalent strain is employed instead of its local counterpart to control the failure mechanism and distribute the released energy over neighboring zones. Besides, the nonlocal damage models are capable of producing mesh-independent and physically meaningful outcomes (Bažant, 1991). More details on the formulations and developments of the phase-field and continuum damage approach can be found in (Dragon *et al*., 2000; Comi and Perego, 2001; Amor *et al*., 2009; Ambati *et al*., 2014; Wu *et al*., 2015; Wang and Waisman, 2016; Vilppo *et al*., 2021).

Applications in fracture modeling within these methods are immensely popular, ranging from brittle fracture (Duda *et al*., 2015; Sargado *et al*., 2018; Janiszewski *et al*., 2019) to quasi-brittle fracture (Bui and Lani, 2011; Nguyen *et al*., 2012;), and ductile fracture (Ambati *et al*., 2015) for two and three-dimensional solid elements, simulation of crack branching (Wolff, 2015) to explicit dynamic damage and phase-field models (Doan *et al*., 2016; Li *et al*., 2016; Doan *et al*., 2017; Ren *et al.*, 2019,) for structures under impact loading conditions, where the load rate notably influences the damage responses. Considering the fracture modeling for thin-walled structures, one can refer to the works of Amiri *et al.* (2014) and Kiendl *et al.* (2016) about phase-field modeling in brittle Kirchoff-Love plates and shells. Gradient-enhanced damage models for thin shells constituted of composite laminates have been studied by Bazilevs *et al.* (2018), Pigazzini *et al.* (2018; 2019). Hosseini *et al.* (2014) presented a quasi-brittle damage description in a solid-like shell model by utilizing isogeometric analysis.

1.1.2 Modeling of heterogeneous materials

Studies on quasi-brittle fracture are based on micromechanics principles and heavily depend on the geometric representation of heterogeneity such as aggregates and air voids (Roy and Gouda, 1973; Lian *et al.*, 2011; Simon and Chandra-Kishen, 2016; Le *et al.*, 2019, Heidari-Rarani and Sayedain, 2019). In general, they aim to assess the influences of parameters such as fracture energy, fatigue properties, and aggregates/voids characteristics (shape, orientation, volume fraction) on the dynamic responses and fracture patterns. A common approach is the family of heterogeneous models which use explicit consideration of rock/voids aggregates (You *et al.*, 2012; Caro *et al.*, 2017; Yang *et al.*, 2017; Suchorzewski *et al.*, 2018; Qin *et al.*, 2020). They are computationally heavy and a considerable part of these elevated computational costs is spent on the modeling of the interface and contact between the particle and the binder. Recent applications (Yilmaz and Molinari, 2017; Heidari-Rarani and Bashadeh-Khodaei-Naeini, 2018) take into account the inclusion of rocks within mortar by representing aggregates as two or three-dimensional ellipse or spheres and utilize the cohesive zone model (CZM) for fracture modeling. Han *et al.* (2018) presents a detailed scanning of air voids and employed the phase-field method to study the fracture process. Whereas, Guo *et al.* (2009) model the material with truss-like elements in a mesoscale computation where the microstructures are generated based on pictures of a real concrete specimen. Alternatively, the methods proposed in (Vanmarcke, 1983; Eliáš *et al.*, 2015; Chen *et al.*, 2018a; Chen *et al.*, 2018b; Castillo *et al.*, 2021) do not explicitly consider aggregate microstructures. Therein, the discretization enables a synthetics representation of the uncertainty of material properties in space and uses repetitive simulations with identical discretization but random differences in terms of material properties. The advantage of this approach is making each simulation manageable enough so that a high number of models can be set up and run while managing to obtain results that are representative of the damage and fracture of the material.

1.1.3 Modeling of microarchitectural solids and structures

Classical continuum theories have been used immensely in the macro-scale analysis of solids in good agreement with experimental outcomes. Nonetheless, when being applied to smaller-scale cases, *e.g.*, materials with either natural or artificial microstructure, composites, and heterogeneous materials, classical approaches show their limitations and fail to capture microstructural effects such as the size effect, *i.e.*, the relationship between external geometric dimensions and internal structures. Multi-scale methods (Massart *et al.*, 2007; Geers *et al.*, 2010; Nguyen *et al.*, 2012) effectively tackle these challenges. However, they significantly increase the problem's complexity and computational cost. This motivates the development of single-scale continuum mechanics theories which boast some multi-scale capabilities when maintaining their homogenizing characteristics (Askes and Aifantis, 2011; Niiranen *et al.*, 2016). Approaches exploiting the simplified theory (Altan and Aifantis, 1997) of Form II of Mindlin's gradient elasticity theory (Mindlin, 1964) have been proved to be applicable to capture size effects by including the strain gradient terms with their stress conjugates into the expression of the internal energy density. In this way, materials with microstructures are treated as continuum media with certain equivalent material properties. The strain gradient elasticity theories have shown their applicability in stress analysis problems beyond the classical linear fracture mechanics, to avoid stress singularity at crack tips (Akarapu and Zbib, 2006). Besides that, high-order strain gradient models also boast their capability of predicting complex mechanical behaviors of pantographic structures (dell'Isola *et al.*, 2019; De Angelo *et al.*, 2019; Spagnuolo *et al.*, 2020; Laudato *et al.*, 2021). In the numerical aspect, the integration of gradient terms demands high-order continuity of the approximated field variables. Therefore, along with theoretical formulations, numerical methods with higher continuity through the domain are developed. Recently, Niiranen *et al.* (2016) have constructed a robust variational formulation of the simplified Mindlin's strain gradient theory based on isogeometric analysis for bar and plane strain/stress problems and numerically implemented through user-defined elements of the commercial software Abaqus (Khakalo *et al.*, 2017). This approach is later adapted to the modeling of beams, plate, and shell structures made of microarchitectural materials (including lattices and auxetics) (Niiranen *et al.,* 2017; Khakalo *et al.*, 2018; Balobanov *et al.*, 2018; Balobanov *et al.*, 2019).

Regarding the fracturing process in this class of materials, continuum damage mechanics appears to be a strong candidate. In recent years, various approaches have been developed for representing the material degradation process under the influences of internal microstructures by different numerical methods. Putar *et al.* (2017) presented a damage model for quasi-brittle materials based on the first strain gradient theory, embedded into the two-dimensional C^1-continuity triangular finite element, which was first derived by Lesicar *et al.* (2014). This type of element consists of three nodes and 36 degrees of freedom such as the displacements and their first and second derivatives concerning the two Cartesian coordinates. A variational strain gradient damage model introduced in (Placidi *et al.,* 2015; Placidi *et al.,* 2018a; Placidi *et al.,* 2018b; Placidi *et al.*, 2020) where governing partial differential equations, boundary conditions, and the Karush-Kuhn-Tucker conditions for damage mechanics are derived from total energy functional. The works in (Yang and Misra, 2010; Wu *et al.*, 2015) utilized the high-order stress-strain theory for damage modeling implemented in an element-free Galerkin method. A generalized damage model was used to simulate quasi-brittle failure in porous media by Mühlich *et al.* (2013), in which the damage parameter corresponds to the void radii. In other words, the void volume fraction increases as damage growth; when the material constitutive relations for porous elastic solids follow the first strain gradient law of the simplified Mindlin's theory (Altan and Aifantis, 1997). Recently, Nguyen and Niiranen (2020) have introduced a single-scale damage model for microarchitectural materials that couples the second strain gradient theory and the evolving damage model (Nguyen *et al.* 2018). The mentioned models show interesting results in predicting damage initiation and propagation. However, thanks to the complicity of materially nonlinear problems, closed-form solutions are essentially nonexistent. Hence, the outcomings from the generalized models can be validated by comparing with experimental results or classical models in which micro architectures are fully modeled.

1.1.4 Modeling of functionally graded structures

Composite functionally graded material (FGM) systems have numerous implementations in engineering. In these materials, the properties vary seamlessly over the geometries. This smooth transition resolves some common problems in multi-material systems with discrete interfaces, such as debonding, stress discontinuity, and thermal stresses due to different thermal expansion between materials (Erdogan and Wu, 1996; Reddy, 2000; Schulz *et al.*, 2003). FGMs also provide an effective way to tailor the material properties to satisfy certain structural requirements while keeping the weight of the structures minimal. In recent years, a wide range of research works within FGM has been accomplished, including bending and eigenproblem studies for graded Euler and Timoshenko beams (Pradhan and Chakraverty, 2013; Su and Banerjee, 2015), experimental validation for bending and vibration of layered beams (Kapuria *et al.*, 2008), structural stability, mechanical and thermal buckling of plates by using the first-order shear deformation theory (Bouazza *et al.*, 2010) and high-order shear deformation theory (Javaheri and Elasmi, 2002). The implementation of a physical neutral surface to represent a functionally graded (FG) plate is mentioned in (Prakash *et al.*, 2009; Lee *et al.*, 2016; Do *et al.*, 2017) in which FG structures with various material arrangements are analyzed, underlying the effectiveness of the proposed formulations by improving the accuracy of the results. Besides that, the fracture behavior of FGMs has been addressed. Comi and Mariani (2007) presented an XFEM simulation of quasi-brittle fracture in various compositions of a glass and epoxy resin, where the material properties are governed by changing the fraction of the glass inclusion in the epoxy matrix. Hirshikesh *et al.* (2019) investigated the crack propagation in alumina-zirconia FGM for different spatial arrangements of the mixture through the phase-field method. Whereas, Torabi and Ansari (2020) analyzed the influences of phase-field parameters on the fracture procedure in functionally graded 2D structures. For shell structures made of an FGM, a phase-field model constructed on a locking-free 7-parameter collocation framework for fracture analysis in FG shells was introduced (Guillén-Hernández, 2020). Recently, Nguyen and Niiranen (2021) proposed a nonlocal damage model for FG plates of high-order shear deformation theory. Experimental results for FG thin-walled structures, however, are relatively sparse. The validation of these dimensionally reduced models can be carried out by comparison with three-dimensional models, which fully represent the spatially varied material properties and undeniably demand much higher computational effort.

1.2 Main contributions

1.2.1 New formulations to improve the accuracy of the nonlocal damage model

This dissertation presents a new formula for the gradient coefficient in the implicit equation of the coupling equivalent strain field to overcome the spurious damage growth problem, which is observed in the conventional damage models. A novel equivalent strain law based on the bi-energy norm is proposed to capture the anisotropic behaviors of quasi-brittle materials under tensile and compressive loading conditions. For better uses of the damage model in practical applications, this work introduces a formulation enabling the model internal parameters such as softening rate and nonlocal interaction length scale to be physically determined from fracture energy which can be measured from experiments. These contributions help to improve the accuracy, performance, and applicability of the damage modeling of quasi-brittle materials.

1.2.2 Implementation of the damage model to study the variability of strain, damage, and fracture in mineral-based materials

In practice, building materials exhibit a wide variability of mechanical properties which significantly affect the performance of structures. The damage model developed in this study is adapted to be capable of modeling heterogeneous materials. It is explored that higher levels of input variability lead to greater possibilities of structural failure and each material parameter contributes differently to the damage behaviors of the tested samples.

1.2.3 Homogenization and damage modeling for micro-architectural materials

It has been shown in the literature that structures made of micro-architectural materials exhibit strong size effects, especially when the size of the internal architectures is comparable to the exterior dimension of the specimens. The proposed damage model is extended to capture these size effects by supplementing the governing equation of the primary variable with the first and second gradient terms of strain to homogenize the micro-architectures.

1.2.4 Development of the damage model for high-order functionally graded plates

The damage model is integrated into the structural model of functionally graded plates of third-order shear deformation theory. The primary field of displacements and the coupling nonlocal equivalent strain field are calculated on the plate's neutral surface which can be notably shifted from the middle surface. The plate stiffness coefficients at every cross-section can be calculated analytically and the integration over plate thickness is not required as in other approaches. This simplification helps to reduce the computational effort significantly. The dimensionally reduced model is capable of predicting adequate structural responses and damage propagation profiles which are demonstrated in several numerical examples. Parametric studies within a variety of FGM configurations are conducted to propose optimal material arrangements, concerning certain external loading conditions.

1.3 Outline of the dissertation

The doctoral dissertation is organized into six Chapters as follows:

- Chapter 2: This chapter presents the formulations of the proposed damage model and its improvements over the previous works.
- Chapter 3: The setup of the heterogeneous panels and their spatially random materials properties are presented. Damage responses of the specimens are analyzed. The relations between the variability of the input parameters and the results are drawn.
- Chapter 4: Homogenization of the micro-architectural materials by the simplified version of Mindlin's strain gradient theory is performed. The damage model for the homogenized materials is presented.
- Chapter 5: Formulations for a third-order shear deformable plate with an integrated damage parameter are derived. Four FGM configurations are designed numerically tested under different load cases. The load-displacement responses of these structures are analyzed to demonstrate the performance of these configurations.
- Chapter 6: The main findings from the works presented in the thesis, their limitations, and recommendations for future research are given.

2. Gradient-enhanced damage model with evolving nonlocal interactions

This chapter comprises a brief description of a gradient damage model including the features that have been developed or improved in the course of Publication 1, including the model formulation, determination of nonlocal interactions, and fracture energy-based damage laws. Weak formulations of the coupling boundary value problem and numerical calculation scheme are also mentioned.

2.1 Formulations of the gradient-enhanced damage model

To describe the nonlinear softening behavior of quasi-brittle materials, a scalar damage parameter $0 \le D \le 1$ is introduced to represent the degradation of material integrity. The elasto-damage energy potential (Lemaitre and Chaboche, 1978) is given by

$$\Psi(\boldsymbol{\varepsilon}, D) = \frac{1}{2}\boldsymbol{\varepsilon}: (1 - D)\mathbb{C}: \boldsymbol{\varepsilon}, \tag{2.1}$$

where $\mathbb{C}$ denotes the four-order elasticity tensor in the intact state, $\boldsymbol{\varepsilon}$ is the second-order elastic strain tensor $\boldsymbol{\varepsilon} = \frac{1}{2}(\nabla\boldsymbol{u} + \boldsymbol{u}\nabla)$ with $\boldsymbol{u}$ denoting the vector of displacements. The stress tensor $\boldsymbol{\sigma}$ and the damage energy release rate Y are obtained by differentiating the free energy potential:

$$\boldsymbol{\sigma} = \frac{\partial\Psi(\boldsymbol{\varepsilon}, D)}{\partial\boldsymbol{\varepsilon}} = (1 - D)\mathbb{C}: \boldsymbol{\varepsilon}, \tag{2.2}$$

$$Y = -\frac{\partial\Psi(\boldsymbol{\varepsilon}, D)}{\partial D} = \frac{1}{2}\boldsymbol{\varepsilon}: \mathbb{C}: \boldsymbol{\varepsilon}. \tag{2.3}$$

The Clausius-Duhem inequality for dissipation (Mazars, 1989) must satisfy the thermodynamics condition:

$$\dot{\phi} = \boldsymbol{\sigma}: \dot{\boldsymbol{\varepsilon}} - \dot{\Psi} = Y\dot{D} \ge 0. \tag{2.4}$$

Since the damage energy release rate Y is nonnegative due to its quadratic form, the nonnegative condition for the damage evolution rate $\dot{D}$ is always satisfied. In the nonlocal damage model presented in this thesis, the damage parameter D is driven by a non-decreasing value κ as

$$D = D(\kappa), \tag{2.5}$$

where κ is the history value of the nonlocal equivalent strain $\bar{\varepsilon}_{eq}$, in other words, the maximum value of $\bar{\varepsilon}_{eq}$ over the whole loading process

$$\kappa = \max(\bar{\varepsilon}_{eq}) \tag{2.6}$$

Damage in a material domain can propagate when the following Kuhn-Tucker conditions are simultaneously satisfied

$$f(\bar{\varepsilon}_{eq}, \kappa) \leq 0, \qquad \dot{D}(\kappa) \geq 0, \qquad f\dot{D} = 0, \tag{2.7}$$

where the loading function $f(\bar{\varepsilon}_{eq}, \kappa) = \bar{\varepsilon}_{eq} - \kappa$ describes the loading states as $f = 0$ is loading and $f < 0$ corresponds to unloading condition. Within the class of quasi-brittle materials, the damage parameter is assumed to follow the exponential rule

$$D = \begin{cases} 0 & \text{if } \kappa < \kappa_0, \\ 1 - \dfrac{\kappa}{\kappa_0}\left[1 - \alpha + \alpha e^{-\beta(\kappa - \kappa_0)}\right] & \text{if } \kappa \geq \kappa_0, \end{cases} \tag{2.8}$$

or the simpler linear law

$$D = \begin{cases} 0 & \text{if } \kappa < \kappa_0, \\ \dfrac{\kappa_0}{\kappa}\left(\dfrac{\kappa - \kappa_0}{\kappa_c - \kappa_0}\right) & \text{if } \kappa_0 \leq \kappa < \kappa_c, \\ 1 & \text{if } \kappa \geq \kappa_c, \end{cases} \tag{2.9}$$

with $1 - \alpha$ being the residual strength of the material in the entirely damaged state. In practice $1 - \alpha$ is set to be a very small value to improve the numerical stability of the solver. And β denotes the softening rate, *i.e.*, the slope of the descending exponential curve. Whereas, κ_c denotes the ultimate strain state corresponding to complete failure.

The nonlocal equivalent strain can be calculated by an explicit or implicit diffusion equation (Peerlings *et al.*, 2001; Peerlings *et al.*, 2004) coupling to the primary governing equation. In this work, the implicit form of second-order is utilized as

$$\bar{\varepsilon}_{eq} - c\nabla^2\bar{\varepsilon}_{eq} = \varepsilon_{eq}, \tag{2.10}$$

where the local equivalent strain ε_{eq} is the intensity of the strain tensor.

2.2 Determination of evolving nonlocal interactions

2.2.1 Anisotropic gradient coefficient

The gradient parameter c in Eq. (2.10) controls the diffusion of the nonlocal equivalent strain which physically represents the zone where micro defects interact inside the material domain. Conventional nonlocal damage models employ a constant value of gradient parameters. These nonlocal approaches can get rid of the mesh dependence problem caused by the local ones. However, they still suffer from spurious damage issues at high levels of deformation and are incapable to predict shear damage bands in compression tests. In this research,

a new formulation of the gradient parameter c is constructed to alleviate the shortcomings of the conventional models (Publication 1).
The implicit diffusion Equation (2.10) is reformulated in a local coordinate (x_1, x_2) which is directed to the principal stresses at a material point as

$$\bar{\varepsilon}_{eq}(x_1, x_2) - \nabla \cdot (\bar{\boldsymbol{c}}\nabla)\bar{\varepsilon}_{eq}(x_1, x_2) = \varepsilon_{eq}(x_1, x_2), \tag{2.11}$$

by using the anisotropic gradient coefficient parameter $\bar{\boldsymbol{c}}$

$$\bar{\boldsymbol{c}} = \begin{bmatrix} c_1 & 0 \\ 0 & c_2 \end{bmatrix} \tag{2.12}$$

with $c_{1,2}$ the evolving coefficients in principal directions:

$$c_{1,2} = c_{1,2}\left(l_c, \varepsilon_{eq}, \sigma_{I,II}\right) = \left(\frac{\kappa_0}{\max\left(\kappa_0, \varepsilon_{eq}\right)}\right)^{\eta} \frac{\sigma_{I,II}^2}{f_t^2} \frac{l_c^2}{2}, \tag{2.13}$$

where κ_0 is the damage threshold in terms of the nonlocal equivalent strain, which is defined as the ratio between the tensile strength f_t and the modulus of elasticity E as $\kappa_0 = f_t/E$. $\sigma_{I,II}$ denote the principal stresses and l_c is the nonlocal interaction length scale. η is a heuristic parameter that provides a possibility to further calibrate the level of the nonlocal interactions. An illustration of the isotropic (obtained by setting $c_1 = c_2 = l_c^2/2$ as in conventional models) and anisotropic nonlocal interaction zones is shown in Figure 1.

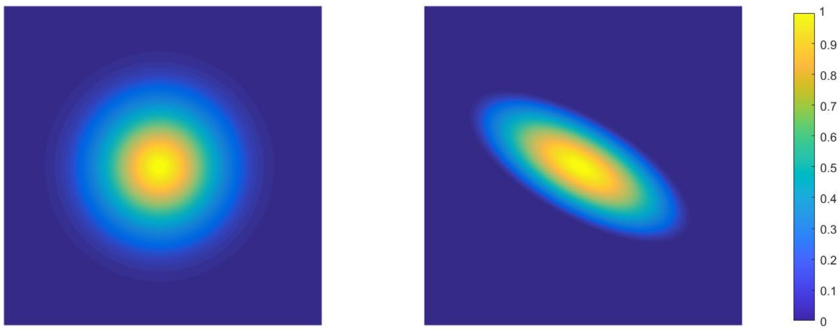

Figure 1. Isotropic (left) and anisotropic (right) diffusions of the nonlocal interactions at a material point (Publication 1, Figure 2); the color code shows the intensity of interactions

2.2.2 Stress smoothing for low-order finite elements

Low-order (linear) elements are commonly utilized in the modeling and simulation of solids and structures because of their simplicity and the relatively small number of degrees of freedom required to build a mesh. That helps to reduce computer memory usage and to save processing time. However, when two low-order fields of displacement and nonlocal equivalent strain are coupled, unphysical stress oscillation is observed. This phenomenon is caused by the mismatch of the two approximated fields as the local equivalent strain is element-wise constant but the nonlocal one is linear (for the case of linear-linear coupling fields) (Simone *et al.*, 2003; Simone *et al.*, 2004). Consequently, the evolving gradient coefficient in Equation (2.13) cannot be obtained correctly from these unphysical stresses. To alleviate this difficulty, a stress smoothing technique based on weighted averaging is proposed (Publication 1).

The smoothed stress is formulated in the form of nonlocal stress as follows:

$$\bar{\boldsymbol{\sigma}}(\boldsymbol{x}) = \frac{\int_\Omega \psi(\boldsymbol{x}-\boldsymbol{\xi})\boldsymbol{\sigma}(\boldsymbol{\xi})d\Omega}{\int_\Omega \psi(\boldsymbol{x}-\boldsymbol{\xi})d\Omega} \tag{2.14}$$

The central idea of the nonlocal concept is to replace the local (oscillating) stress field with its nonlocal counterpart by using weighted averaging over a neighboring space of the point of interest, whose coordinates are $\boldsymbol{x}$ and $\boldsymbol{\xi}$ denoting the coordinate of its adjacent points in the material domain Ω. The weight function ψ can be selected as the Gauss distribution

$$\psi(\boldsymbol{x}-\boldsymbol{\xi}) = \exp\left(-\frac{\|\boldsymbol{x}-\boldsymbol{\xi}\|^2}{2l_c^2}\right), \tag{2.15}$$

or the bell-shaped function, which contains a cutoff of the surrounding points when positioning outside a circular region of radius r

$$\psi(\boldsymbol{x}-\boldsymbol{\xi}) = \begin{cases} \left[1-\frac{\|\boldsymbol{x}-\boldsymbol{\xi}\|^2}{r^2}\right]^2 & \text{if } \|\boldsymbol{x}-\boldsymbol{\xi}\| \le r \\ 0 & \text{otherwise} \end{cases}. \tag{2.16}$$

Figure 2 depicts the one-dimensional Gauss distribution functions in comparison with the bell-shape weight functions with different cutoff radii ($r_1 = l_c, r_2 = 2l_c, r_3 = 3l_c$). A three-dimensional function of Gauss distribution is also plotted in the figure.

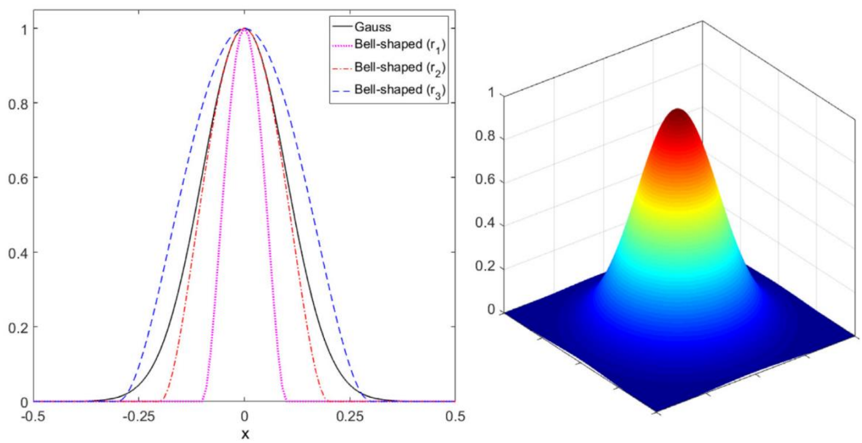

Figure 2. 1-Dimensional weight functions (left); 3-Dimensional view of the Gauss distribution function (right) (Publication 1, Figure 1).

The principal values $\bar{\sigma}_{I,II}$ of the smoothed stress $\bar{\boldsymbol{\sigma}}$ are used in the calculation of the evolving gradient parameter in Equation (2.13) in the case of linear-linear coupling fields instead of $\sigma_{I,II}$. Figure 3 boasts the effectiveness of the presented stress smoothing technique via an example of a bar under tension (see Section 4, Publication 1). It can be seen that no ill stress profile is observed when using the Gauss distribution weight function or a bell-shaped function with $r = 2l_c$. For higher orders (quadratic and beyond) of the fields, the stress oscillation is significantly less severe, as analyzed in (Verhoosel *et al.*, 2011; Cuomo *et al.*, 2014; Tran *et al.*, 2016) with IGA and confirmed in (Bui *et al.*, 2016) with FEM. Therefore, the stress smoothing is not necessary to be performed in the isogeometric analysis of the homogenized micro-architectural materials (Publication 3) and the third-order plates (Publication 4) due to their high-order approximations.

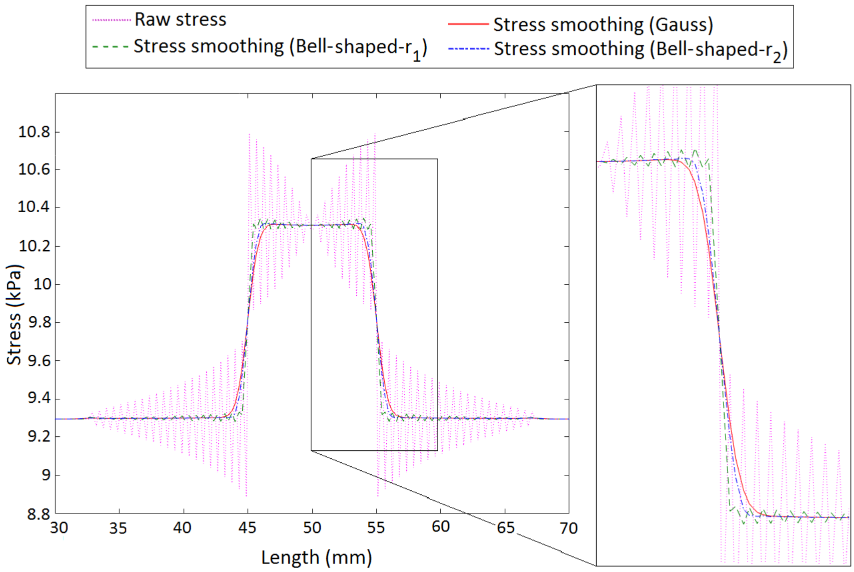

Figure 3. Stress oscillation and smoothed stresses by Gauss distribution and bell-shaped functions with $r_1 = l_c$ and $r_2 = 2l_c$ (Publication 1, Figure 8).

2.3 Damage evolution laws based on fracture energy

In the family of nonlocal damage models, the nonlocal interaction length scale parameter l_c plays a crucial role as it controls the width of the damage band and more importantly the global response of structures. However, it is still unclear that l_c would be treated as a material or a model parameter included to overcome the mesh dependence problem of local damage models (Wu and Nguyen, 2018). Hence, a direct method to measure the value of l_c is arguably impractical. In previous studies (Peerlings *et al.*, 1996; Geers *et al.*, 1998; Giry *et al.*, 2011; Saroukhani *et al.*, 2013; Poh and Sun, 2017, Negi, 2020), the nonlocal interaction length parameter has been given intuitively, regarding material characteristics, *e.g.*, three times the size of the largest aggregate in concrete, or estimated based on the exterior size of the tested specimen (Jirásek *et al.*, 2004). Nguyen *et al.* (Publication 1) propose a formula to determine the length scale parameter from a physical quantity, fracture energy, as a relation between the length scale, the fracture energy, and the rate of softening. This formula is applicable by assuming that the damage evolution follows an exponential law. Motivated by the works of Volokoh (2012, 2013), in Publication 2, an improved formulation that can be applied for different rules of damage evolution in quasi-brittle materials (*e.g.* linear softening) is derived.

Considering a cube of material, the edge length of which is l_c, as shown in Figure 4. When the cube is completely damaged, with ω denoting the volumetric work of fracture, the total dissipated energy of the whole volume is equal to ωl_c^3. The work density ω corresponds to the area limited by the horizontal axis and the stress-strain curve of a uniaxial tension test from the rest state until the complete failure.

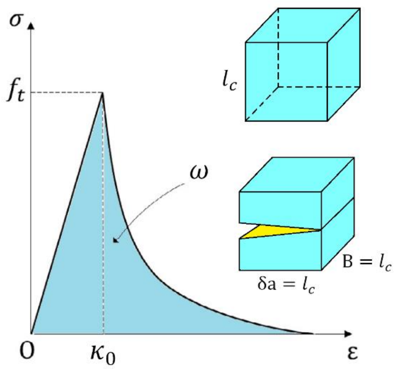

Figure 4. Schematic of the relation between the volumetric and surface work of fracture.

For the two damage evolution laws mentioned in Equation (2.8) and Equation (2.9), the respective volumetric work of fracture is calculated as

$$\omega_{exp} = \frac{E\kappa_0^2}{2} + \frac{E\kappa_0}{\beta}, \tag{2.17}$$

and

$$\omega_{lin} = \frac{E\kappa_0\kappa_c}{2}. \tag{2.18}$$

On the other hand, the energy required to form the new crack surfaces thorough the cube of edge length l_c is equal to $G_F l_c^2$, where the fracture energy is defined as the surface work of fracture. By equating the two energy expressions as

$$G_F l_c^2 = \omega l_c^3, \tag{2.19}$$

the damage evolution laws are tied to the corresponding nonlocal interaction length scale parameters by the following relations

$$l_{c,exp} = \frac{2G_F}{E\kappa_0\left(\frac{\kappa_0}{2} + \frac{1}{\beta}\right)}, \tag{2.20}$$

and

$$l_{c,lin} = \frac{G_F}{E\kappa_0\kappa_c}. \tag{2.21}$$

In comparison to the formula proposed by Nguyen *et al.* (2018) (see Publication 1, Equation 30), the relation in Equation 2.20 includes the contribution of the elastic energy stored in the material domain, *i.e.*, $E\kappa_0^2/2$. Nevertheless, in practical applications (see Publication 4, Figure 13c), these energy terms (the area under the elastic part of the stress-strain curve) is substantially smaller than the external work of fracture (the area under the softening part of the stress-strain curve). By ignoring the elastic term in Equation (2.20), the two formulas are identical.

2.4 Bi-energy-norm based equivalent strain

In the class of strain-driven damage models, the equivalent strain, as a scalar intensity of the strain tensor, has a strong impact on the damage propagation because it defines the damage surface which is the limit of the elastic regime in both stress and strain spaces. For quasi-brittle materials, the laws of the equivalent strain namely Mazars (Mazars, 1989), smooth Rankine (Jirásek and Bauer, 2012), and the modified von Mises (de Vree *et al.*, 1995) are commonly used. In this subchapter, these formulas are reviewed with their pros and cons, then a novel bi-energy-based equivalent strain law is presented.

Mazar's model takes into account the positive parts of the strain tensor as follows:

$$\varepsilon_{eq}(\boldsymbol{\varepsilon}) = \sqrt{\sum_{I=1}^{3} \langle \varepsilon_I \rangle^2}, \qquad I = 1,2,3, \tag{2.22}$$

with ε_I denoting the principal strains and $\langle \blacksquare \rangle$ being the Macauley bracket which extracts the positive value of a quantity: $\langle \blacksquare \rangle = (|\blacksquare| + \blacksquare)/2$.
The smooth Rankine equivalent strain is defined based on the scaled norm of the positive parts of the effective stress tensor, *i.e.*, $\widehat{\boldsymbol{\sigma}} = \mathbb{C}:\boldsymbol{\varepsilon}$, as

$$\varepsilon_{eq}(\boldsymbol{\varepsilon}) = \frac{1}{E}\sqrt{\sum_{I=1}^{3} \langle \widehat{\boldsymbol{\sigma}}_I(\boldsymbol{\varepsilon}) \rangle^2}, \qquad I = 1,2,3, \tag{2.23}$$

where $\widehat{\boldsymbol{\sigma}}_I$ are the effective principal stresses. The Mazar's and smooth Rankine rules are simple and have been well implemented in tension-dominated problems. Nonetheless, they are not able to capture crushing damage neither shear bands caused by compressive loads. That leads to the proposal of the modified von Mises equivalent strain law

$$\varepsilon_{eq}(\boldsymbol{\varepsilon}) = \frac{k-1}{2k(1-\nu)} I_1 + \frac{1}{2k}\sqrt{\sum_{I=1}^{3} \frac{(k-1)^2}{(1-2\nu)^2} I_1^2 + \frac{12k}{(1-\nu)^2} J_2}, \tag{2.24}$$

Where $I_1(\boldsymbol{\varepsilon})$ and $J_2(\boldsymbol{\varepsilon})$ are the first invariant of the strain tensor and the second invariant of the deviatoric strain tensor, respectively. ν indicates the Poisson's ratio and k is a model parameter included to normalize the influences of the tensile and compressive parts of the strain tensor. By setting k equal to the ratio between the compressive strength and tensile strength of materials, the modified von Mises law can deal with a wide range of quasi-brittle materials such as concrete ($k = 10\sim15$) and limestone ($k = 7\sim10$). However, in certain cases such as the test of an L-shaped panel (Publication 1, Section 5.2), the von Mises strain fails to predict the structural response when underestimating the peak loading capacity of the panel by 15%.

This research introduces a new formula to calculate the equivalent strain based on the bi-energy norm which in turn is obtained by decomposing the strain tensor into a positive part $\boldsymbol{\varepsilon}^+$ and a negative part $\boldsymbol{\varepsilon}^-$ as

$$\boldsymbol{\varepsilon}^+ = \varepsilon_{ij}^+ = \sum_{m=1}^{3} \langle \varepsilon^{\boldsymbol{m}} \rangle \tilde{n}_i^m \, \tilde{n}_j^m, \tag{2.25}$$

where $\varepsilon^{\boldsymbol{m}}$ stands for the m^{th} principal strain and $\tilde{n}_i^m$ is the unit vector in the m^{th} principal direction.

$$\boldsymbol{\varepsilon}^- = \boldsymbol{\varepsilon_p} - \boldsymbol{\varepsilon}^+, \tag{2.26}$$

with ε_p being the principal strain. Correspondingly, the equivalent values of the two decomposed strain tensors are calculated in terms of energy norms

$$\varepsilon_{eq}^{\pm}(\boldsymbol{\varepsilon}) = \frac{1}{\sqrt{E}} \sqrt{\boldsymbol{\varepsilon}^{\pm} : \mathbb{C} : \boldsymbol{\varepsilon}^{\pm}}. \tag{2.27}$$

Then the bi-energy norm equivalent strain law is composed as

$$\varepsilon_{eq}(\boldsymbol{\varepsilon}) = \frac{k\varepsilon_{eq}^+ + \varepsilon_{eq}^-}{\lambda(k+1)}, \tag{2.28}$$

where λ is an empirical parameter, which scales the size of the damage surface, providing a way to further calibrate the model responses. In comparison to the aforementioned formulations, the bi-energy norm equivalent strain approximately matches the von Mises and smooth Rankine in the tensile zone (the top right quadrant in Figure 5), resulting in a better approximation of the damage behaviors of the L-shaped specimen in Publication 1, Section 5.2, while obsesses a possibility to be utilized within various quasi-brittle materials.

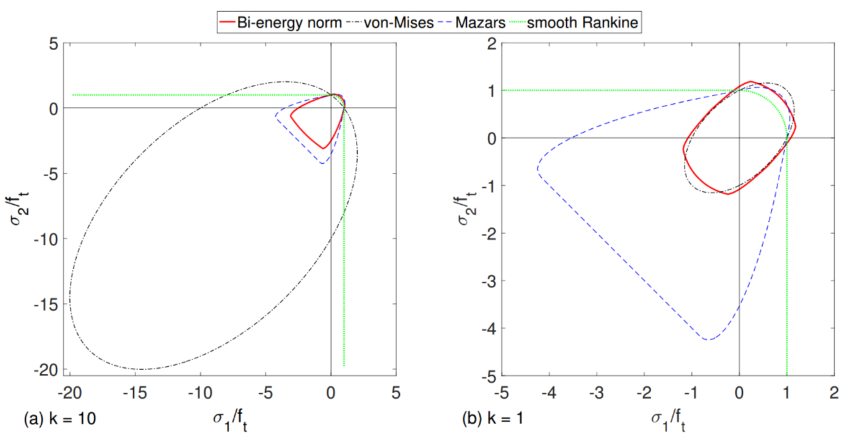

Figure 5. Plane stress equivalent strains in principal stress space with different brittleness (Publication 1, Figure 5).

2.5 Weak forms of the damage model for solids

The boundary value problem in a solid domain Ω is expressed as

$$\begin{aligned} &\nabla \cdot \boldsymbol{\sigma} + \boldsymbol{b} = \boldsymbol{0} && \text{in } \Omega \\ &\boldsymbol{u} = \bar{\boldsymbol{u}} && \text{on } \Gamma_u \\ &\boldsymbol{\sigma} \cdot \boldsymbol{n} = \bar{\boldsymbol{t}} && \text{on } \Gamma_t \end{aligned} \tag{2.29}$$

where $\boldsymbol{b}$ represents the body force vector, $\bar{\boldsymbol{u}}$ is the vector of enforced displacements over the essential boundary Γ_u and $\bar{\boldsymbol{t}}$ denotes the tractions on the natural boundary Γ_t, respectively. $\boldsymbol{n}$ is the normal vector of Γ_t.
The variational formulations of the boundary value problem are stated as follows: for $\boldsymbol{b} \in [L^2(\Omega)]^3$ and $\boldsymbol{t} \in [L^2(\Omega)]^3$, find $\boldsymbol{u} \in \boldsymbol{U} \subset [H^1(\Omega)]^3$ such that

$$a_u(\boldsymbol{u}, \boldsymbol{v}) = l_u(\boldsymbol{v}) \quad \forall\, \boldsymbol{v} \in \boldsymbol{V} \subset [H^1(\Omega)]^3, \tag{2.30}$$

where the bilinear form $a_u\colon \boldsymbol{U} \times \boldsymbol{V} \to \mathbb{R}$ and the load functional $l_v\colon \boldsymbol{V} \to \mathbb{R}$ are defined as

$$a_u(\boldsymbol{u}, \boldsymbol{v}) = \int_\Omega [(1 - D)\boldsymbol{\varepsilon}(\boldsymbol{u})\colon \mathbb{C}\colon \boldsymbol{\varepsilon}(\boldsymbol{v})]\, d\Omega, \tag{2.31}$$

and

$$l_u(\boldsymbol{v}) = \int_\Omega \boldsymbol{b} \cdot \boldsymbol{v}\, d\Omega + \int_{\Gamma_t} \bar{\boldsymbol{t}} \cdot \boldsymbol{v}\, d\Gamma. \tag{2.32}$$

The weak form of the implicit equation of the nonlocal equivalent strain is formulated in the same manner: for $e \in L^2(\Omega)$ find $\bar{\varepsilon}_{eq} \in \bar{\mathcal{E}} \subset [H^1(\Omega)]^3$ such that

$$a_e(\bar{\varepsilon}_{eq}, e) = c \quad \forall\, e \in \mathcal{E} \subset H^1(\Omega), \tag{2.33}$$

with the bilinear form

$$a_e(\bar{\varepsilon}_{eq}, e) = \int_\Omega [\bar{\varepsilon}_{eq} e + \nabla \bar{\varepsilon}_{eq} (\boldsymbol{c} \nabla e)]\, d\Omega, \tag{2.34}$$

and the analogous load functional

$$l_e(e) = \int_\Omega \varepsilon_{eq} e\, d\Omega. \tag{2.35}$$

Numerically, the weak formulations of the nonlocal damage model for homogeneous isotropic solids presented in Equations (2.30~2.35) required approximation functions of C^0-continuity. Therefore, the finite element method with linear Lagrange basis functions is applied.

2.6 Scheme for numerical solutions

The governing systems of equations at an equilibrium state are written as the balance between the internal and external forces:

$$\begin{aligned} \boldsymbol{f}_{int}^{u} &= \boldsymbol{f}_{ext}^{u}, \\ \boldsymbol{f}_{int}^{e} &= \boldsymbol{f}_{ext}^{e}, \end{aligned} \tag{2.36}$$

where the superscripts u and e correspond to the primary variable of displacements and the coupling nonlocal equivalent strain. The internal forces are derived from the bilinear forms of the boundary value problem, whereas, the load functionals result in the external forces.
In an incremental form, the field variables at the current step $k+1$ are calculated from a linearized system of equations based on the converged solutions of the previous step k as

$$\begin{aligned} \delta\boldsymbol{f}_{int,k+1}^{u} &= \boldsymbol{f}_{ext,k+1}^{u} - \boldsymbol{f}_{int,k}^{u}, \\ \delta\boldsymbol{f}_{int,k+1}^{e} &= \boldsymbol{f}_{ext,k+1}^{e} - \boldsymbol{f}_{ext,k}^{e}, \end{aligned} \tag{2.37}$$

Denoting $\delta\widehat{\boldsymbol{d}}$ and $\delta\hat{\boldsymbol{e}}$ as the incremental solutions of the displacement and nonlocal equivalent strain, respectively, the left-hand side of the incremental Equation (2.37) is separated as

$$\begin{aligned} \boldsymbol{K}_t^{uu}\delta\widehat{\boldsymbol{d}} + \boldsymbol{K}_t^{ue}\delta\hat{\boldsymbol{e}} &= \boldsymbol{f}_{ext,k+1}^{u} - \boldsymbol{f}_{int,k}^{u}, \\ \boldsymbol{K}_t^{eu}\delta\widehat{\boldsymbol{d}} + \boldsymbol{K}_t^{ee}\delta\hat{\boldsymbol{e}} &= \boldsymbol{f}_{ext,k+1}^{e} - \boldsymbol{f}_{ext,k}^{e}, \end{aligned} \tag{2.38}$$

where the tangent stiffnesses are obtained by differentiating the internal forces:

$$\begin{aligned} \boldsymbol{K}_t^{uu} &= \frac{\partial \boldsymbol{f}_{int}^{u}}{\delta\widehat{\boldsymbol{d}}}, \\ \boldsymbol{K}_t^{ue} &= \frac{\partial \boldsymbol{f}_{int}^{u}}{\delta\hat{\boldsymbol{e}}}, \\ \boldsymbol{K}_t^{eu} &= \frac{\partial \boldsymbol{f}_{int}^{e}}{\delta\widehat{\boldsymbol{d}}}, \\ \boldsymbol{K}_t^{ee} &= \frac{\partial \boldsymbol{f}_{int}^{e}}{\delta\hat{\boldsymbol{e}}}. \end{aligned} \tag{2.39}$$

Arranging Equation (2.38) in a matrix form yields:

$$\begin{bmatrix} \boldsymbol{K}_t^{uu} & \boldsymbol{K}_t^{uu} \\ \boldsymbol{K}_t^{uu} & \boldsymbol{K}_t^{uu} \end{bmatrix}_k \begin{bmatrix} \delta\widehat{\boldsymbol{d}} \\ \delta\hat{\boldsymbol{e}} \end{bmatrix}_{k+1} = \begin{bmatrix} \boldsymbol{f}_{ext}^{u} \\ \boldsymbol{f}_{ext}^{e} \end{bmatrix}_{k+1} - \begin{bmatrix} \boldsymbol{f}_{int}^{u} \\ \boldsymbol{f}_{int}^{e} \end{bmatrix}_k \tag{2.40}$$

Then, the incremental equation is iteratively solved by employing the displacement-controlled Newton-Raphson method.

The presented damage model is verified through a variety of numerical examples by convergence studies within different discretization configurations, *i.e.*, element sizes and types, under different boundary and loading conditions. For model validation, the results are compared with that of other numerical methods as well as experiments, showing good agreement (see Sections 4 and 5 of Publication 1).

3. Study of variability of strain, damage, and fracture in concrete

This chapter summarized the main work of Publication 2. The evolving nonlocal damage model is employed to explore the numerical simulations of nonlocal strain, damage, and fracture in a typical quasi-brittle material in civil engineering such as concrete, which is treated as heterogeneous thanks to its complicated ingredients. The research considers the isolated contribution of two spatially random properties, being crucial in the fracture process: the elasticity modulus (E) and the tensile strength (f_t).

3.1 Methodology

The procedure of modeling the spatial variability of mechanical properties is conducted in three steps.

3.1.1 Defining the domain geometry and mesh

Two geometries as shown in Figure 6 are used in this study: a square plate of side 200 mm with a central hole of diameter 40 mm and an L-shaped panel with 500 mm height. Both the plates have a thickness of 100 mm.

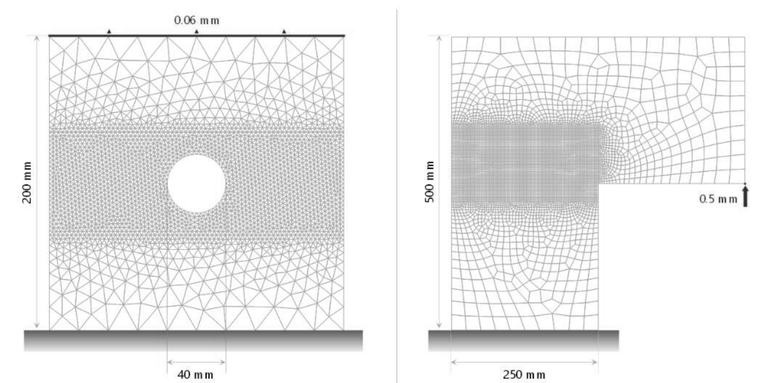

Figure 6. Geometries and boundary conditions of the tested specimens: Holed panel (left); L-shaped panel (right) (Publication 3, Figure 1).

External loads are imposed on the two geometries in terms of prescribed displacements. The boundary conditions and loading configurations are chosen to

induce different damage/failure mechanisms in the two plates: pure tensile damage in the holed plate and mix-mode damage in the L-shaped plate.
The two plates are generated and meshed by using the open-source software Gmsh (Geuzaine and Remacle, 2009). The mesh orientations are set to be random so that the nodes and elements do not align with the weakest section of the plates. The holed plate consists of linear triangular (T3) elements while the L-shaped plated is discretized with linear quadrilateral (Q4) elements. The meshes of the two plates are locally refined where the damage paths are predicted to propagate through. The two plates are tested with different mesh sizes from $2\ mm$ to $5\ mm$ in the refined zones and an optimal size of $3\ mm$ is selected to ensures mesh independent results while saving computational effort.

3.1.2 Assigning material properties

For each specimen of the two types of geometries, two spatially random sets of material properties, *i.e.*, the modulus of elasticity E and the tensile strength f_t are generated following the standard distribution rule, by using the matrix decomposition method reported by (El-Kadi and Williams, 2000). In total, 400 specimens in four groups are generated with geometric types and material properties as shown in Table 1, with E_μ and f_t_μ denoting the mean values and E_σ and f_t_σ being the standard deviations.

Table 1. Material parameters of the specimens.

Geometry type	Number of specimens	E_μ (GPa)	E_σ (GPa)	f_t_μ (MPa)	f_t_σ (MPa)
Holed	100	20	1.5	2	0
Holed	100	20	0	2	1.5
L-shaped	100	20	1.5	2.7	0
L-shaped	100	20	0	2.7	0.2025

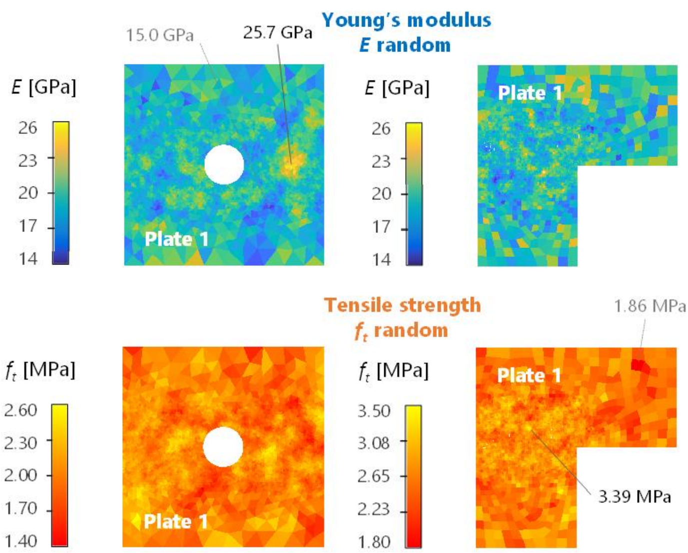

Figure 7. Example random fields of material properties in a holed plate and an L-shaped plate.

The random fields of parameters are assigned to the specimens in an element-wise manner where every element possesses a unique set of E and f_t based on the coordinates of its geometric center. Exemplary random fields of Young's modulus and tensile strength of a holed plate and an L-shaped are illustrated in Figure 7. It is worth noting that the values of the two random fields are not repeatable over all the specimens.

3.1.3 Finite element simulations for localized strain and damage

The evolving gradient damage model introduced in Publication 1 is utilized herein and adapted to tackle the simulation of the 400 random specimens made of heterogeneous materials.

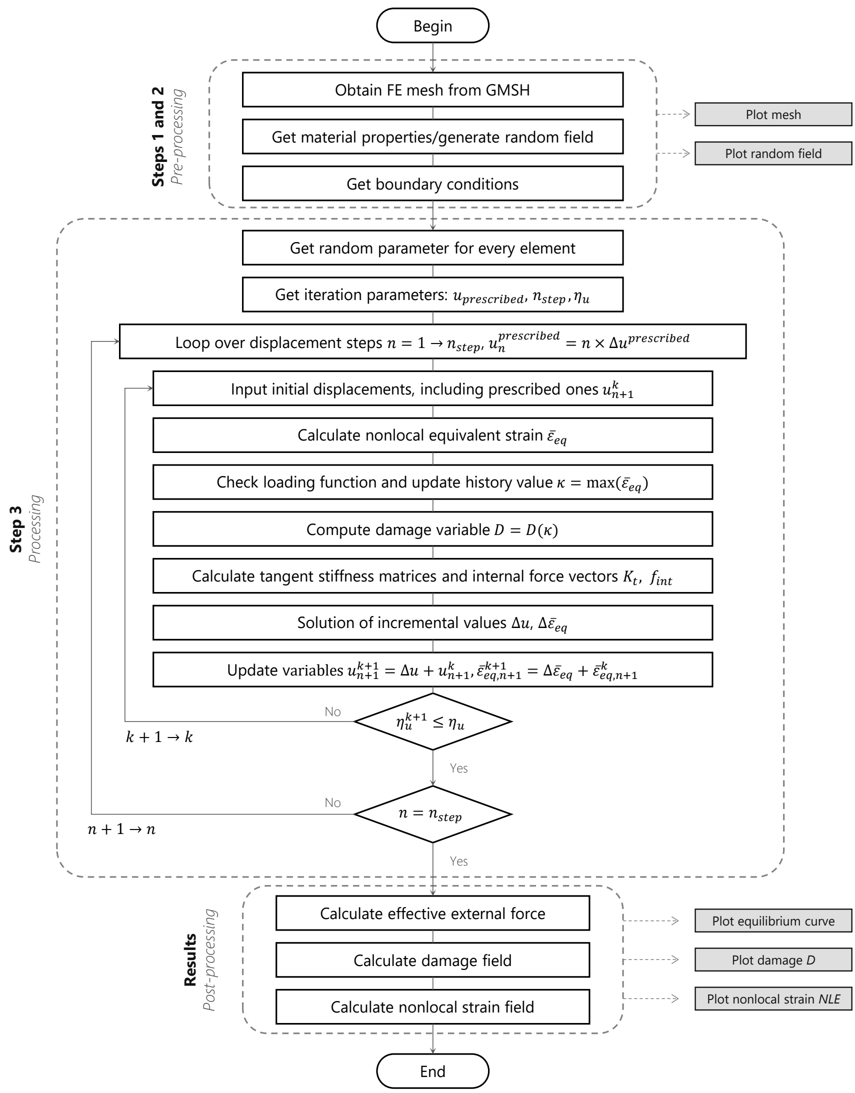

Figure 8. Calculation scheme for the random specimens of heterogeneous materials by using the evolving gradient damage model (Publication 3, Figure 3).

For each simulation, the random material properties are mapped from the corresponding random field to the elements in the mesh of a specimen. Outcomings of the calculation such as the localized strain, the damage profile, and the reaction force at the displacement-prescribed points are stored for further analyses. The whole computation process comprising of the above steps is depicted in Figure 8 as a flow chart.

3.2 Analysis of the simulation results

Damage behaviors of the specimens of the two geometries are collected and analyzed in comparison with two homogeneous (fixed values of both E and f_t) panels. The outcomings can be categorized into three types: force-displacement response, localized strain and damage, and fracture path. The corresponding statistical quantities such as mean, standard deviation, and coefficient of variation are derived.

3.2.1 Force-displacement responses

The simulation results reveal that the spatial variations in terms of E and f_t differently contribute to the force-displacement curves. For both types of geometries, the variability of tensile strength does not show any effect in the elastic regime but leads to much higher dispersion (3~4 times) than that of the elasticity modulus when damage is propagating.

The probability that the peak loading capacity of a random specimen exceeds that of a homogeneous plate is consistently smaller than 50% for all the studied cases. This observation suggests that material heterogeneity weakens structures; in other words, it increases the probability of failure of structures. Hence, numerical calculations may overestimate structural integrity by assuming that materials are homogeneous.

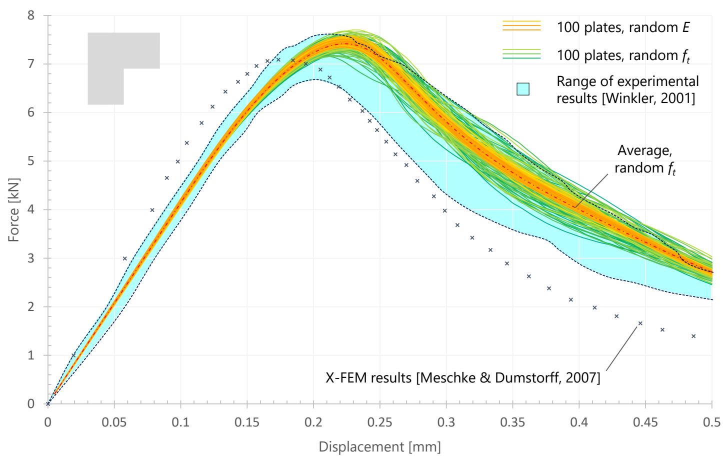

Figure 9. Comparison of the structural responses for an L-shaped concreted plate, including results from experiment and XFEM (Publication 3, Figure 6).

The force-displacement curves of the L-shaped panel, with both variabilities of E and f_t almost fall inside the *experimental zone* reported by Meschke and Dummstorff (2007) as shown in Figure 9. This finding confirms the ability of this numerical simulation approach to offer an inexpensive alternative to the laboratory results.

3.2.2 Strain and damage

Observations from the nonlocal equivalent strain and damage profiles in all the specimens show that the variability of Young's modulus has a low influence on the overall results, while the tensile strength variability contributes substantially. For both of the two geometries, the average profiles approach to which obtained from the homogeneous domains.

High uncertainty zones locate at the frontier of the damaged areas, and progress as the damage propagates. In general, the uncertainty in damage and localized strain increase in the later steps of the loading procedure.

3.2.3 Failure paths

The failure paths in this research are constructed by connecting the nodes with maximum nonlocal equivalent strain to generate shaper fracture lines that represent the actual macro cracks. The wandering of these paths is plotted in Figure 10 for the holed plate and in Figure 11 for the L-shaped plate.

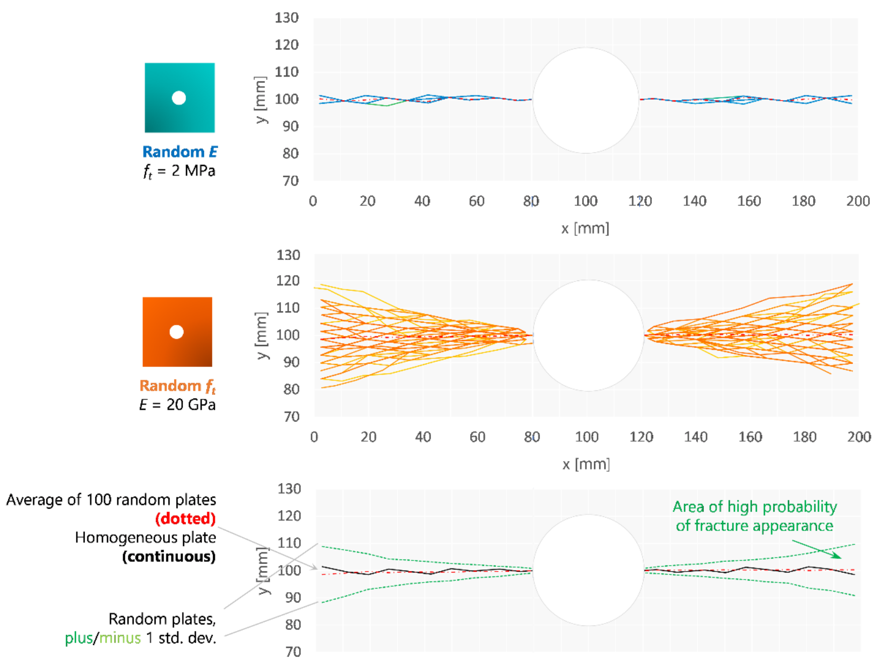

Figure 10. Comparison of the fracture paths for a holed plate (Publication 3, Figure 11).

The variability of the tensile strength results in many diverse fracture paths for both geometries. In the holed plate, the fracture path of the homogeneous specimen shows some zagged line segments due to the way it is constructed, depending on the position of the nodes in the unstructured mesh. However, the average path of the random specimens is nearly horizontal, which matches the theoretical crack line of the homogeneous plate. In the L-shaped panel, the average fracture path is close to that of the homogeneous specimens and well compared to the experimental result (Winkler, 2001).

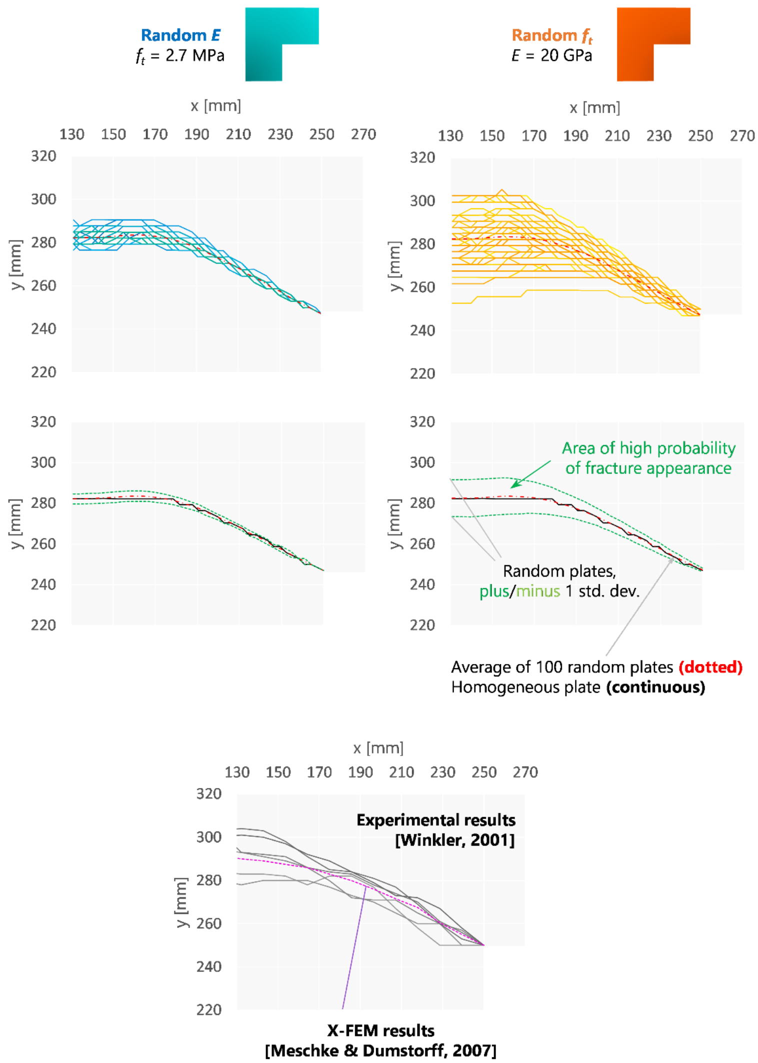

Figure 11. Comparison of the fracture paths for an L-shaped plate, including results from experiment and XFEM (Publication 3, Figure 12).

4. Second strain gradient damage modeling of quasi-brittle materials with microarchitectures

The evolving nonlocal damage model proposed in Publication 1 is extended to cope with micro-architectural materials, as presented in detail in Publication 3. Developed according to the simplified Mindlin's theory, the elasto-damage energy potential contains not only the classical strain but the first and second gradient terms as well. The numerical implementation is performed within the framework of isogeometric analysis to exploit the higher continuity of the NURBS basis functions.

4.1 Second strain gradient homogenization

The free energy potential in Equation (2.1) is enriched with higher-order strain energy terms and written in a tensorial form by

$$\begin{aligned}\Psi(\boldsymbol{\varepsilon},\boldsymbol{\mu},\boldsymbol{\gamma},D) = \frac{1}{2}\boldsymbol{\varepsilon}:(1-D)\mathbb{C}:\boldsymbol{\varepsilon} + \frac{1}{2}\boldsymbol{\mu} \mathrel{\vdots} (1-D)\mathbb{C}_1 \mathrel{\vdots} \boldsymbol{\mu} \\ + \frac{1}{2}\boldsymbol{\gamma} :: (1-D)\mathbb{C}_2 :: \boldsymbol{\gamma},\end{aligned} \tag{4.1}$$

The first product term represents the classical elasto-damage energy in damage mechanics. Whereas, the second and third terms are nonlocal internal energy corresponding to the third-order and fourth-order micro deformation tensors, which are denoted by $\boldsymbol{\mu}$ and $\boldsymbol{\gamma}$, respectively. Notation $\mathbb{C}_1$ and $\mathbb{C}_2$, accordingly, denotes the sixth-order and eight-order tensor of elastic moduli. The contraction operators are built in such a way that Equation (4.1) can be rewritten in the index notation as follows

$$\begin{aligned}\Psi = \frac{1}{2}\varepsilon_{ij}(1-D)\mathbb{C}^{ijkl}\varepsilon_{kl} + \frac{1}{2}\mu_{ijk}(1-D)\mathbb{C}_1^{ijklmn}\mu_{lmn} \\ + \frac{1}{2}\gamma_{ijkl}(1-D)\mathbb{C}_2^{ijklmnpq}\gamma_{mnpq}.\end{aligned} \tag{4.2}$$

Form II of Mindlin's theory defines $\boldsymbol{\mu}$ as the first gradient and $\boldsymbol{\gamma}$ as the second gradient of the macroscopic strain tensor:

$$\boldsymbol{\mu} = \nabla\boldsymbol{\varepsilon} \text{ and } \boldsymbol{\gamma} = \nabla\nabla\boldsymbol{\varepsilon}. \tag{4.3}$$

The work conjugates of the strain tensors $\boldsymbol{\varepsilon}, \boldsymbol{\mu}$, and $\boldsymbol{\gamma}$, *i.e.*, the classical stress $\boldsymbol{\sigma}$, the double stress $\boldsymbol{\tau}$, and the triple stress $\boldsymbol{\beta}$ are derived by partial differentiation of the free energy potential:

$$\boldsymbol{\sigma} = \frac{\partial\Psi(\boldsymbol{\varepsilon}, \boldsymbol{\mu}, \boldsymbol{\gamma}, D)}{\partial\boldsymbol{\varepsilon}} = (1-D)\mathbb{C}\colon \boldsymbol{\varepsilon}, \tag{4.4}$$

$$\boldsymbol{\tau} = \frac{\partial\Psi(\boldsymbol{\varepsilon}, \boldsymbol{\mu}, \boldsymbol{\gamma}, \boldsymbol{D})}{\partial\boldsymbol{\mu}} = (1-D)\mathbb{C}_1 \,\vdots\, \boldsymbol{\mu}, \tag{4.5}$$

$$\boldsymbol{\beta} = \frac{\partial\Psi(\boldsymbol{\varepsilon}, \boldsymbol{\mu}, \boldsymbol{\gamma}, \boldsymbol{D})}{\partial\boldsymbol{\beta}} = (1-D)\mathbb{C}_2 :: \boldsymbol{\gamma}. \tag{4.6}$$

The damage energy release rate Y is obtained in the same manner:

$$Y = -\frac{\partial\Psi(\boldsymbol{\varepsilon}, \boldsymbol{\mu}, \boldsymbol{\gamma}, D)}{\partial D} = \frac{1}{2}\boldsymbol{\sigma}\colon \boldsymbol{\varepsilon} + \frac{1}{2}\boldsymbol{\tau} \,\vdots\, \boldsymbol{\mu} + \frac{1}{2}\boldsymbol{\beta} :: \boldsymbol{\gamma}. \tag{4.7}$$

The Clausius-Duhem inequality for dissipation has to satisfy the following thermodynamics condition:

$$\dot{\phi} = \boldsymbol{\sigma}\colon \dot{\boldsymbol{\varepsilon}} + \boldsymbol{\tau} \,\vdots\, \dot{\boldsymbol{\mu}} + \boldsymbol{\beta} :: \dot{\boldsymbol{\gamma}} - \dot{\Psi} = Y\dot{D} \geq 0. \tag{4.8}$$

Similar to the case of classical elasticity presented in Chapter 2, herein, the damage energy release rate Y is non-negative so that the condition for damage evolution $\dot{D} \geq 0$ always holds. Based on the simplified (one-parameter) form of Mindlin's theory (Altan and Aifanis, 1997), the double stress $\boldsymbol{\tau}$ and the triple stress $\boldsymbol{\beta}$ can be reduced to

$$\boldsymbol{\tau} = g_1^2 \nabla\boldsymbol{\sigma} \text{ and } \boldsymbol{\beta} = g_2^4 \nabla\nabla\boldsymbol{\sigma}\,, \tag{4.9}$$

where g_1 and g_2 stand for the length parameters, which characterize the influence of the micro-architectures.

Under the principle of virtual work, the virtual internal energy of a body Ω is given by

$$\delta W_{int} = \int_{\Omega} (\boldsymbol{\sigma}\colon \delta\boldsymbol{\varepsilon} + \boldsymbol{\tau} \,\vdots\, \delta\boldsymbol{\mu} + \boldsymbol{\beta} :: \delta\boldsymbol{\gamma}) d\Omega, \tag{4.10}$$

Substitution of Equations (4.4~4.6) and (4.9) into Equation (4.10) yields the virtual internal energy of a damaged body Ω

$$\begin{aligned} \delta W_{int} = \int_{\Omega} [(1-D)(\boldsymbol{\varepsilon}\colon \mathbb{C}\colon \delta\boldsymbol{\varepsilon} + g_1^2 \nabla(\mathbb{C}\colon \boldsymbol{\varepsilon}) \,\vdots\, \delta\nabla\boldsymbol{\varepsilon} \\ + g_2^4 \nabla\nabla(\mathbb{C}\colon \boldsymbol{\varepsilon}) :: \delta\nabla\nabla\boldsymbol{\varepsilon}\, d\Omega \end{aligned} \tag{4.11}$$

The damage parameter D is driven by the nonlocal equivalent strain $\bar{\varepsilon}_{eq}$ which is calculated through the implicit diffusion Equation (2.10).

Remark 1: The two length parameters g_1 and g_2 represent the length scale parameters enabling to capture the size effects constituted by microarchitectures. They are, in essence, distinguishing from the nonlocal interaction length scale l_c which models the influences of micro defects in the damage process.

4.2 Weak forms and isogeometric analysis

4.2.1 Weak forms of the nonlocal damage problems with micro-architectural materials

By employing the second strain gradient formulations, the material domains with micro-architectures can be treated as solids and coupled with the evolving nonlocal damage model presented in Chapter 2. For simplicity, the nonclassical external loads are omitted. The weak form of the second strain gradient damage problem is given as follows: for $\boldsymbol{b} \in [L^2(\Omega)]^3$ and $\boldsymbol{t} \in [L^2(\Omega)]^3$, find $\boldsymbol{u} \in \boldsymbol{U} \subset [H^3(\Omega)]^3$ such that

$$a_u(\boldsymbol{u}, \boldsymbol{v}) = l_u(\boldsymbol{v}) \quad \forall\, \boldsymbol{v} \in \boldsymbol{V} \subset [H^3(\Omega)]^3, \tag{4.12}$$

where the bilinear form $a_u\colon \boldsymbol{U} \times \boldsymbol{V} \to \mathbb{R}$ and the load functional $l_v\colon \boldsymbol{V} \to \mathbb{R}$ are defined as

$$\begin{aligned} a_u(\boldsymbol{u}, \boldsymbol{v}) = \int_\Omega \, &[(1 - D)(\boldsymbol{\varepsilon}(\boldsymbol{u})\colon \mathbb{C}\colon \boldsymbol{\varepsilon}(\boldsymbol{v}) + g_1^2 \nabla\big(\mathbb{C}\colon \boldsymbol{\varepsilon}(\boldsymbol{u})\big) \,\vdots\, \nabla\boldsymbol{\varepsilon}(\boldsymbol{v}) \\ &+ g_2^4 \nabla\nabla(\mathbb{C}\colon \boldsymbol{\varepsilon}(\boldsymbol{u})) :: \nabla\nabla\boldsymbol{\varepsilon}(\boldsymbol{v}))] d\Omega, \end{aligned} \tag{4.13}$$

and

$$l_u(\boldsymbol{v}) = \int_\Omega \boldsymbol{b} \cdot \boldsymbol{v} \, d\Omega + \int_{\Gamma_t} \bar{\boldsymbol{t}} \cdot \boldsymbol{v} \, d\Gamma. \tag{4.14}$$

The weak form of the implicit diffusion equation of the nonlocal equivalent strain is inherited from Equations (2.33~2.35).

4.2.2 Basics of Isogeometric Analysis

The numerical modeling of the second strain gradient elasticity requires C^2-continuity over element boundary, that the traditional FEM with Lagrange or Hermite polynomial basis functions is not capable of without additional degrees of freedom, *e.g.*, derivatives the primary variable, resulting in much more demanding numerical models which require a huge amount of computer memory and processing ability. Alternatively, isogeometric analysis (IGA) with the non-uniform B-spline (NURBS) basis functions can be exploited.

IGA was introduced by Hughes *et al.* (2005) to bridge the gap between computer-aided design (CAD) and computer-aided engineering (CAE). In modern CAD software, complex geometries, *e.g.*, free-form surfaces and watertight connectors, are built with NURBS functions because of their "exact geometry" feature. In IGA, geometries imported from CAD are meshed exactly by the same functions as they were constructed on, unlike the polynomial approximation in FEM. That nicely eliminates the discretization errors caused by the mismatch of the stages in the design and analysis process, in addition to the higher continuity of the NURBS shape functions, as mentioned above. These two unique features over FEM make IGA gain more popularity in research and commercial applications recently.

The NURBS description of a three-dimensional body Ω in a parametric space (ξ,η,ζ) is given as a geometrical mapping between the parameter space and the physical space $[0,1]^3 \rightarrow \Omega$:

$$\boldsymbol{S}(\xi,\eta,\zeta) = \sum_{i=1}^{n_\xi}\sum_{j=1}^{m_\eta}\sum_{k=1}^{l_\zeta} R_{i,j,k}^{p,q,r}(\xi,\eta,\zeta)\boldsymbol{P}_{i,j,k} \tag{4.15}$$

where $\boldsymbol{P}_{i,j,k}$; $i = 1,\dots,n_\xi; j = 1,\dots,m_\eta; k = 1\dots,l_\zeta$ denotes the vector of control point coordinates. $R_{i,j,k}^{p,q,r}(\xi,\eta,\zeta)$ is a three-dimensional NURBS basis functions of order p,q,r defined as

$$R_{i,j,k}^{p,q,r}(\xi,\eta,\zeta) = \frac{N_{i,p}(\xi)N_{j,q}(\eta)N_{k,r}(\zeta)w_{i,j,k}}{\sum_{\hat{\imath}=1}^{n}\sum_{\hat{\jmath}=1}^{m}\sum_{\hat{k}=1}^{l} N_{\hat{\imath},p}(\xi)N_{\hat{\jmath},q}(\eta)N_{\hat{k},r}(\zeta)w_{\hat{\imath},\hat{\jmath},\hat{k}}}. \tag{4.16}$$

Herein, the independent univariate B-spline basis functions $N_{i,p}$, $N_{j,q}$, and $N_{k,r}$ of order p,q, and r, respectively, are constructed by using the Cox-de Boor recursive formula:

$$N_{i,0}(\xi) = \begin{cases} 1 & \text{if } \xi_i \le \xi < \xi_{i+1}, \\ 0 & \text{otherwise,} \end{cases} \tag{4.17}$$

$$N_{i,p}(\xi) = \frac{\xi-\xi_i}{\xi_{i+p}-\xi_i}N_{i,p-1}(\xi) + \frac{\xi_{i+p+1}-\xi}{\xi_{i+p+1}-\xi_{i+1}}N_{i+1,p-1}(\xi), \tag{4.18}$$

where ξ_i denotes the coordinates of element boundaries in the parametric space $\xi \in [0,1]$ characterized by a knot vector $\Xi = \{\xi_1,\xi_2,\dots,\xi_{n+p+1}\}$; $\xi_i \le \xi_{i+1}$; $i = 1,2,\dots,n+p$.

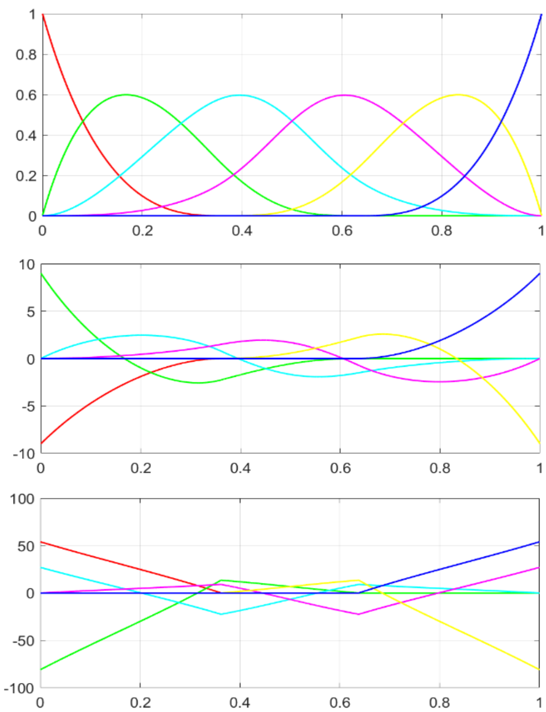

Figure 12. Univariate 3rd-order B-spline basis functions for a knot vector $\Xi = \{0,0,0,0,1,1,1,1\}$ and their first and second derivatives (top to bottom) (Publication 3, Figure 3)

The NURBS basis functions of order p provide up to C^{p-1}-continuity over element (knot span) boundaries; and generally, a geometry approximated by three-dimensional NURBS basis functions of 3rd-order assures C^2-continuity in the whole domain, which is beneficial in the context of the second strain elasticity. For the illustration of this advantage, a sample set of B-spline basis functions and their derivatives is depicted in Figure 12.

4.3 Numerical examples

In this subchapter, a parametric study of square panels subjected to compressive load is conducted to demonstrate the applicability of the second strain gradient damage model in capturing the size effects of microarchitectural materials. This example is studied in detail in Section 5 of Publication 3 which includes other benchmarks and examples as well, *e.g.*, a one-dimensional bar under tension and a plane stress L-shaped panel undergoing mixed-mode fracture. The geometry and boundary conditions of the panel are depicted in Figure 13 and the bulk material parameters are listed in Table 2.

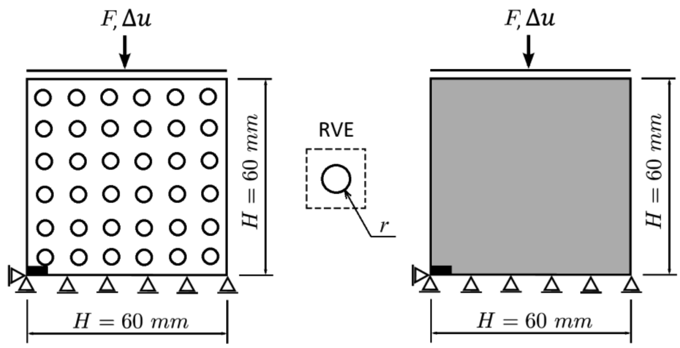

Figure 13. Geometry and boundary conditions of a microarchitectural plate (left), a representative element (middle), and a homogenized plate by the second strain gradient theory (right). The black area in the bottom left corner is slightly weakened to trigger the damage.

Table 2. Bulk material properties of the specimen.

Property	Description	Value
E	Modulus of elasticity	20 GPa
υ	Poisson's ratio	0.2
f_t	Tensile strength	2 MPa
l_c	Nonlocal damage interaction parameter	3 mm
G_F	Fracture energy	13 N/m
k	Compressive/tensile strength	1

The plates contain circular holes with various radii while keeping the same volume fraction of the voids, i.e., the ratio between the radius of a hole and edge length of a representative element (RVE). These micro architectures are homogenized by employing the second strain gradient theory (Equation (4.11)) with the length parameters $g_{1,2}$ corresponding to the hole radii. Numerically, the homogenized plates are analyzed in the framework of IGA with the third-order NURBS basis functions, and their damage propagation profiles are illustrated in Figure 14. Whereas, reference solutions (in Figure 15) with explicitly modeled holes are carried out by using the smoothing damage model in Publication 1 with linear quadrilateral (Q4) finite elements.

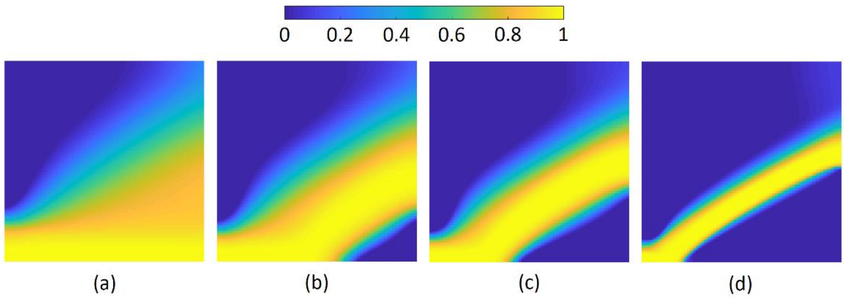

Figure 14. Damage profiles in plates, homogenized by the second strain gradient theory with different values of the gradient parameters: (a) $g_1 = g_2 = 2.5\ mm$; (b) $g_1 = g_2 = 1.5\ mm$; (c) $g_1 = g_2 = 1.0\ mm$; (d) $g_1 = g_2 = 0.5\ mm$ (Publication 3, Figure 20)

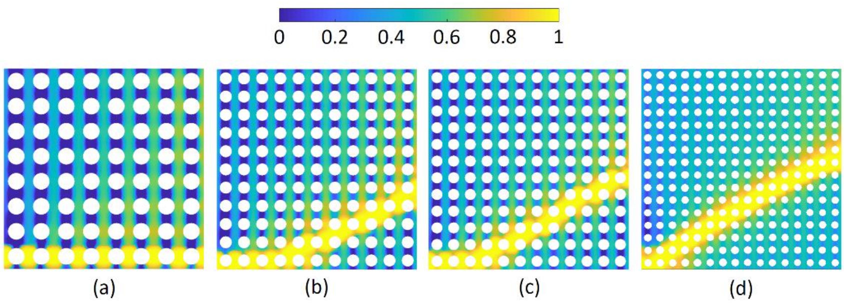

Figure 15. Damage profiles in plates with different size of micro architectures: (a) $r = 1.9\ mm$; (b) $r = 1.4\ mm$; (c) $r = 1.3\ mm$; (d) $r = 0.9\ mm$ (Publication 3, Figure 24)

Comparison of the results reveals substantial size effects of the internal architectures on the damage behaviors: when the sizes of the hole are closer to the exterior size of the domain ($r = 1.9\ mm$ and $g_1 = g_2 = 2.5\ mm$), the plates fail by crushing damage (Figures 14a and 15a). Whereas, in cases of the smaller micro architectures, shear band formations are found (Figures 14d and 15d) and the damage behaviors tend to which of the homogeneous plate.

5. Damage modeling of third-order functionally graded plates

This chapter covers the main contents of Publication 4. In which, the evolving nonlocal damage model has been integrated into the formulations of third-order shear deformable plates which are made of functionally graded quasi-brittle material. The concept of the neutral plane is utilized and a single damage parameter is defined for each plate cross-section, enabling the analytical computation of the plate stiffness coefficients. The numerical solutions of the problem are solved by using isogeometric analysis.

5.1 Plates of functionally graded materials

5.1.1 Material descriptions

Considering a bi-material plate domain where the material proportions continuously alter along with its thickness direction (Z-axis), as illustrated in Figure 16a. Two types of material arrangements are defined: in an asymmetric configuration (Figures 16b, 16c), the top surface of the plate consists of material 1, whereas the whole bottom is made of material 2. The proportions of each material, denoted by V_1 and V_2, are given by

$$V_1 = \left(\frac{z}{h} + \frac{1}{2}\right)^n ;\ V_2 = 1 - V_1. \tag{5.1}$$

The symmetric or sandwich arrangement (Figures 13d, 13e) is set up as follows:

$$V_1 = \left|\frac{2z}{h}\right|^n ;\ V_2 = 1 - V_1, \tag{5.2}$$

where $n \geq 0$ is the exponent coefficient that controls the kind of material mixture. The rule of mixture (Reddy, 2000) defines the variation of material properties over the plate thickness as

$$P(z) = (P_1 - P_2)V_1 + P_2 = P_1V_1 + P_2V_2, \tag{5.3}$$

with P_1 and P_2 denote any properties of materials 1 and 2, respectively. $P(z)$ is the corresponding properties of the mixtures varying in the Z-direction.

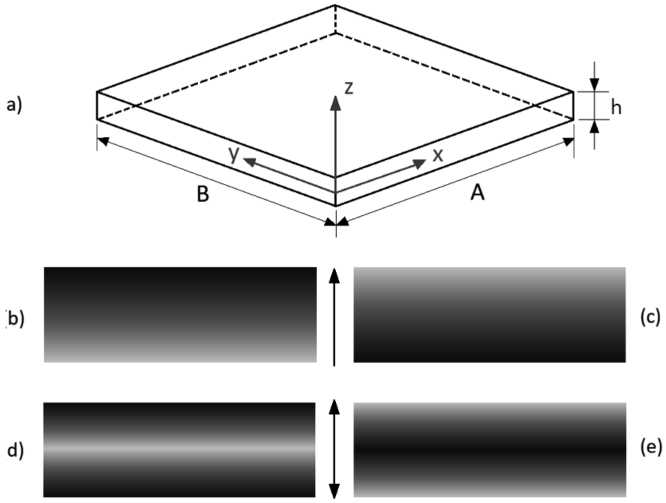

Figure 16. Functionally graded plates within different material configurations (Publication 4, Figure 1)

5.1.2 The physical neutral surface

In asymmetric functionally graded plates, due to the change in material properties, the stress distribution over the plate thickness is different from that of homogeneous or symmetric plates. Consequently, the plane where the stresses vanish is shifted from the geometrical middle surface of the plates and the equilibrium of stress resultants is no longer satisfied. To alleviate this problem, the neutral surface is introduced as a reference plane for deformation based on the equilibrium of forces.

The physical neutral surface of an inhomogeneous plate is determined so that integration of the first moment of elasticity modulus in the thickness direction is equal to zero

$$\int_{-h/2}^{h/2} E(z)(z - z_0)dz = 0. \tag{5.4}$$

Thus, the position of the neutral surface is obtained as

$$z_0 = \frac{\int_{-h/2}^{h/2} E(z)zdz}{\int_{-h/2}^{h/2} E(z)dz}. \tag{5.5}$$

Moreover, the dimensionless location of the plate neutral surface can be defined as follows:

$$\frac{z_0}{h} = \frac{n(E_1 - E_2)}{2(n+2)(E_1 + nE_2)}. \tag{5.6}$$

5.2 Damage modeling of FGM-HSDT plates with von Kármán strains

5.2.1 Dimensional reduction model

The displacements $\boldsymbol{u} = (u, v, w)$ of an arbitrary point inside the plate domain are given in terms of the translational and rotational movements of the corresponding point in the neutral surface (x, y, z_0) as cubic functions of the thickness coordinate z:

$$\begin{aligned} u(x,y,z) &= u_0(x,y,z_0) + (z - z_0)\phi_x + (z - z_0)^3 d_1(w_{,x} + \phi_x), \\ v(x,y,z) &= v_0(x,y,z_0) + (z - z_0)\phi_y + (z - z_0)^3 d_1(w_{,y} + \phi_y), \\ w(x,y,z) &= w_0(x,y), \end{aligned} \tag{5.7}$$

with $d_1 = -\frac{4}{3h^2}$. (u_0, v_0, w_0) denote the translations and (ϕ_x, ϕ_y) are the rotations of the neutral surface.

This plate model takes into account the geometrical nonlinearity by employing von Kármán's formulation (Reddy, 1990) where the transversal (bending) and the in-plane (stretching) deformations are coupled. Accordingly, the non-zero strain components read:

$$\begin{aligned} \varepsilon_{xx} &= u_{0,x} + \frac{1}{2} w_{0,x}^2 + (z - z_0)\phi_{x,x} + (z - z_0)^3 d_1(w_{0,xx} + \phi_{x,x}), \\ \varepsilon_{yy} &= v_{0,y} + \frac{1}{2} w_{0,y}^2 + (z - z_0)\phi_{y,y} + (z - z_0)^3 d_1(w_{0,yy} + \phi_{y,y}), \\ \gamma_{yz} &= w_{0,y} + \phi_y + 3(z - z_0)^2 d_1(w_{0,y} + \phi_y), \\ \gamma_{xz} &= w_{0,x} + \phi_x + 3(z - z_0)^2 d_1(w_{0,x} + \phi_x), \\ \gamma_{xy} &= u_{0,y} + v_{0,x} + w_{0,x} w_{0,y} + (z - z_0)(\phi_{x,y} + \phi_{y,x}) \\ &\quad + (z - z_0)^3 d_1(\phi_{x,y} + w_{0,xy} + \phi_{y,x} + w_{0,yx}) \end{aligned} \tag{5.8}$$

Rewriting the kinematic relations in a vectorial form yield:

$$\boldsymbol{\varepsilon} = \boldsymbol{\varepsilon}_b^0 + \boldsymbol{\varepsilon}_s^0 + (z - z_0)\boldsymbol{\varepsilon}^1 + (z - z_0)^2 \boldsymbol{\varepsilon}^2 + (z - z_0)^3 \boldsymbol{\varepsilon}^3, \tag{5.9}$$

where $\boldsymbol{\varepsilon} = [\varepsilon_{xx}, \varepsilon_{yy}, \gamma_{yz}, \gamma_{xz}, \gamma_{xy}]^{\boldsymbol{T}}$ and the tensors of the non-zero strain components are denoted as

$$\boldsymbol{\varepsilon}_b^0 = \begin{bmatrix} \varepsilon_{xx}^0 \\ \varepsilon_{yy}^0 \\ \gamma_{xy}^0 \end{bmatrix} = \begin{bmatrix} u_{0,x} + \frac{1}{2} w_{0,x}^2 \\ v_{0,y} + \frac{1}{2} w_{0,y}^2 \\ u_{0,y} + v_{0,x} + w_{0,x} w_{0,y} \end{bmatrix},$$

$$\boldsymbol{\varepsilon}_s^0 = \begin{bmatrix} \gamma_{yz}^0 \\ \gamma_{xz}^0 \end{bmatrix} = \begin{bmatrix} w_{0,y} + \phi_y \\ w_{0,x} + \phi_x \end{bmatrix},$$

$$\boldsymbol{\varepsilon}^1 = \begin{bmatrix} \varepsilon_{xx}^1 \\ \varepsilon_{yy}^1 \\ \gamma_{xy}^1 \end{bmatrix} = \begin{bmatrix} \phi_{x,x} \\ \phi_{y,y} \\ \phi_{x,y} + \phi_{y,x} \end{bmatrix},$$

$$\boldsymbol{\varepsilon}^2 = \begin{bmatrix} \gamma_{yz}^2 \\ \gamma_{xz}^2 \end{bmatrix} = 3d_1 \begin{bmatrix} w_{0,y} + \phi_y \\ w_{0,x} + \phi_x \end{bmatrix},$$

$$\boldsymbol{\varepsilon}^3 = \begin{bmatrix} \varepsilon_{xx}^3 \\ \varepsilon_{yy}^3 \\ \gamma_{xy}^3 \end{bmatrix} = d_1 \begin{bmatrix} w_{0},_{xx} + \phi_{x,x} \\ w_{0},_{yy} + \phi_{y,y} \\ \phi_{x,y} + w_{0},_{xy} + \phi_{y,x} + w_{0},_{yx} \end{bmatrix}, \tag{5.10}$$

with the superscripts of the strain tensors indicating their indices.
The plate is assumed to be in the plane stress state whose elasticity matrices are given by

$$\mathbb{C}_0(z) = \frac{E_0(z)}{1-(\nu(z))^2} \begin{bmatrix} 1 & \nu(z) & 0 \\ \nu(z) & 1 & 0 \\ 0 & 0 & \dfrac{1-\nu(z)}{2} \end{bmatrix},$$

$$\mathbb{G}_0(z) = G_0(z) \begin{bmatrix} 1 & 0 \\ 0 & 1 \end{bmatrix} \tag{5.11}$$

with $E_0(z)$ being Young's modulus and $G_0(z) = \frac{\mathrm{E}_0(z)}{2(1+\nu)}$ standing for the out-of-plane shear modulus in the intact state of the mixture of the functionally graded material, depending on the thickness coordinate as depicted in Equation (5.3); and ν stands for the Poisson ratio. Accordingly, the plate stiffness coefficients are defined as follows

$$\{\mathbb{A}, \mathbb{B}, \mathbb{D}\} = \int_{-h/2}^{h/2} \{1, (z - z_0), (z - z_0)^2\} \mathbb{C}_0(z) dz,$$

$$\{\mathbb{F}_1, \mathbb{F}_2, \mathbb{F}_3\} = \int_{-h/2}^{h/2} \{(z - z_0)^3, (z - z_0)^4, (z - z_0)^6\} \mathbb{C}_0(z) dz\,,$$

$$\{\mathbb{H}_1, \mathbb{H}_2, \mathbb{H}_3\} = \int_{-h/2}^{h/2} \{1, (z - z_0)^2, (z - z_0)^4\} \mathbb{G}_0(z) dz\,, \tag{5.12}$$

5.2.2 Incorporation of the nonlocal damage formulations into the plate model

In the softening regime, when the nonlocal equivalent strain at a certain point inside the plate domain exceed the damage threshold κ_0, the damage parameter D is introduced into the expressions of material parameters

$$E(z) = (1 - D)\mathrm{E}_0(z),$$

$$G(z) = (1 - D)G_0(z), \tag{5.13}$$

Herein, D is driven by the coupling field of nonlocal equivalent strain given in Equation (2.10) where its right-hand side term, *i.e.*, the local equivalent strain on the plate neutral surface, is interpolated from the ones on the top and bottom surfaces by

$$\varepsilon_{eq}(z_0) = \frac{1}{h}\left[\left(\frac{h}{2} - z_0\right) \varepsilon_{eq}^T + \left(\frac{h}{2} + z_0\right) \varepsilon_{eq}^B\right], \tag{5.14}$$

with $\varepsilon_{eq}^T = \varepsilon_{eq}\left(\frac{h}{2}\right)$ and $\varepsilon_{eq}^B = \varepsilon_{eq}\left(-\frac{h}{2}\right)$ being the equivalent values calculated from the strains on the top and bottom surfaces.

The force resultants are derived from the above kinematic conditions and the constitutive relations as

$$\boldsymbol{N} = (1-D)\big(\mathbb{A}\boldsymbol{\varepsilon}_b^0 + \mathbb{B}\boldsymbol{\varepsilon}^1 + \mathbb{F}_1\boldsymbol{\varepsilon}^3\big),$$

$$\boldsymbol{M} = (1-D)\big(\mathbb{B}\boldsymbol{\varepsilon}_b^0 + \mathbb{D}\boldsymbol{\varepsilon}^1 + \mathbb{F}_2\boldsymbol{\varepsilon}^3\big),$$

$$\boldsymbol{P} = (1-D)\big(\mathbb{F}_1\boldsymbol{\varepsilon}_b^0 + \mathbb{F}_2\boldsymbol{\varepsilon}^1 + \mathbb{F}_3\boldsymbol{\varepsilon}^3\big),$$

$$\boldsymbol{Q} = (1-D)(\mathbb{H}_1\boldsymbol{\varepsilon}_s^0 + \mathbb{H}_2\boldsymbol{\varepsilon}^2),$$

$$\boldsymbol{R} = (1-D)(\mathbb{H}_2\boldsymbol{\varepsilon}_s^0 + \mathbb{H}_3\boldsymbol{\varepsilon}^2), \tag{5.15}$$

where $\boldsymbol{N}, \boldsymbol{M}, \boldsymbol{P}, \boldsymbol{Q}, \boldsymbol{R}$ denote the membrane forces, the bending moments, the higher-order moments, the out-of-plane shear forces, and the higher-order out-of-plane shear forces, respectively. Following the principle of virtual work, the virtual strain energy of the plate is given by

$$\begin{aligned}
\delta W_{int} &= \int_\Omega \int_{-h/2}^{h/2} \sigma_{ij}\varepsilon_{ij}\,dz\,d\Omega \qquad i,j = x,y,z \\
&= \int_\Omega (\boldsymbol{N}^T\delta\boldsymbol{\varepsilon}_b^0 + \boldsymbol{M}^T\delta\boldsymbol{\varepsilon}^1 + \boldsymbol{P}^T\delta\boldsymbol{\varepsilon}^3 + \boldsymbol{Q}^T\delta\boldsymbol{\varepsilon}_s^0 + \boldsymbol{R}^T\delta\boldsymbol{\varepsilon}^2)\,d\Omega \\
&= \int_\Omega (1-D)\{[(\boldsymbol{\varepsilon}_b^0)^T\mathbb{A}\delta\boldsymbol{\varepsilon}_b^0 + (\boldsymbol{\varepsilon}^1)^T\mathbb{B}\delta\boldsymbol{\varepsilon}_b^0 + (\boldsymbol{\varepsilon}^3)^T\mathbb{F}_1\delta\boldsymbol{\varepsilon}_b^0] \\
&\quad + [(\boldsymbol{\varepsilon}_b^0)^T\mathbb{B}\delta\boldsymbol{\varepsilon}^1 + (\boldsymbol{\varepsilon}^1)^T\mathbb{D}\delta\boldsymbol{\varepsilon}^1 + (\boldsymbol{\varepsilon}^3)^T\mathbb{F}_2\delta\boldsymbol{\varepsilon}^1] \\
&\quad + [(\boldsymbol{\varepsilon}_b^0)^T\mathbb{F}_1\delta\boldsymbol{\varepsilon}^3 + (\boldsymbol{\varepsilon}^1)^T\mathbb{F}_2\delta\boldsymbol{\varepsilon}^3 + (\boldsymbol{\varepsilon}^3)^T\mathbb{F}_3\delta\boldsymbol{\varepsilon}^3] \\
&\quad + [(\boldsymbol{\varepsilon}_s^0)^T\mathbb{H}_1\delta\boldsymbol{\varepsilon}_s^0 + (\boldsymbol{\varepsilon}^2)^T\mathbb{H}_2\delta\boldsymbol{\varepsilon}_s^0] \\
&\quad + [(\boldsymbol{\varepsilon}_s^0)^T\mathbb{H}_2\delta\boldsymbol{\varepsilon}^2 + (\boldsymbol{\varepsilon}^2)^T\mathbb{H}_3\delta\boldsymbol{\varepsilon}^2]\}d\Omega
\end{aligned} \tag{5.16}$$

5.2.3 Weak forms of the plate damage problem

The variational formulations of the primary field boundary problem read as follows: for $\boldsymbol{f} \in [L^2(\Omega)]^3$, $\boldsymbol{F} \in [L^2(\Omega)]^3$, and $\boldsymbol{M} \in [L^2(\Omega)]^2$, find $\boldsymbol{u} = (u, v, w) \in \boldsymbol{\mathcal{U}} \subset [H^2(\Omega)]^3$ and $\boldsymbol{\phi} = (\phi_x, \phi_y) \in \boldsymbol{\Phi} \subset [H^1(\Omega)]^2$ such that

$$a(\boldsymbol{u}, \hat{\boldsymbol{u}}; \boldsymbol{\phi}, \hat{\boldsymbol{\phi}}) = l(\hat{\boldsymbol{u}}, \hat{\boldsymbol{\phi}}) \qquad \begin{aligned} &\forall\, \hat{\boldsymbol{u}} = (\hat{u}, \hat{v}, \hat{w}) \in \hat{\boldsymbol{\mathcal{U}}} \subset [H^2(\Omega)]^3 \\ &\text{and } \hat{\boldsymbol{\phi}} = (\hat{\phi}_x, \hat{\phi}_y) \in \hat{\boldsymbol{\Phi}} \subset [H^1(\Omega)]^2, \end{aligned} \tag{5.17}$$

where the bilinear form a: $(\boldsymbol{\mathcal{U}} \times \boldsymbol{\Phi}) \times (\hat{\boldsymbol{\mathcal{U}}} \times \hat{\boldsymbol{\Phi}}) \to \mathbb{R}$ and the load functional l: $(\hat{\boldsymbol{\mathcal{U}}} \times \hat{\boldsymbol{\Phi}}) \to \mathbb{R}$ are defined as

$$\begin{aligned}
a(\boldsymbol{u}, \hat{\boldsymbol{u}}; \boldsymbol{\phi}, \hat{\boldsymbol{\phi}}) &= \int_\Omega (1-D)\{[(\boldsymbol{\varepsilon}_b^0)^T\mathbb{A}\delta\hat{\boldsymbol{\varepsilon}}_b^0 + (\boldsymbol{\varepsilon}^1)^T\mathbb{B}\hat{\boldsymbol{\varepsilon}}_b^0 + (\boldsymbol{\varepsilon}^3)^T\mathbb{F}_1\hat{\boldsymbol{\varepsilon}}_b^0] \\
&\quad + \big[(\boldsymbol{\varepsilon}_b^0)^T\mathbb{B}\hat{\boldsymbol{\varepsilon}}^1 + (\boldsymbol{\varepsilon}^1)^T\mathbb{D}\hat{\boldsymbol{\varepsilon}}^1 + (\boldsymbol{\varepsilon}^3)^T\mathbb{F}_2\hat{\boldsymbol{\varepsilon}}^1\big] \\
&\quad + \big[(\boldsymbol{\varepsilon}_b^0)^T\mathbb{F}_1\hat{\boldsymbol{\varepsilon}}^3 + (\boldsymbol{\varepsilon}^1)^T\mathbb{F}_2\hat{\boldsymbol{\varepsilon}}^3 + (\boldsymbol{\varepsilon}^3)^T\mathbb{F}_3\hat{\boldsymbol{\varepsilon}}^3\big] \\
&\quad + \big[(\boldsymbol{\varepsilon}_s^0)^T\mathbb{H}_1\hat{\boldsymbol{\varepsilon}}_s^0 + (\boldsymbol{\varepsilon}^2)^T\mathbb{H}_2\hat{\boldsymbol{\varepsilon}}_s^0\big] \\
&\quad + \big[(\boldsymbol{\varepsilon}_s^0)^T\mathbb{H}_2\hat{\boldsymbol{\varepsilon}}^2 + (\boldsymbol{\varepsilon}^2)^T\mathbb{H}_3\hat{\boldsymbol{\varepsilon}}^2\big]\}d\Omega,
\end{aligned} \tag{5.18}$$

with $\boldsymbol{\varepsilon}_b^0 = \boldsymbol{\varepsilon}_b^0(\boldsymbol{u}, \boldsymbol{\phi})$, $\boldsymbol{\varepsilon}_s^0 = \boldsymbol{\varepsilon}_s^0(\boldsymbol{u}, \boldsymbol{\phi})$, $\boldsymbol{\varepsilon}^1 = \boldsymbol{\varepsilon}^1(\boldsymbol{u}, \boldsymbol{\phi})$, $\boldsymbol{\varepsilon}^2 = \boldsymbol{\varepsilon}^2(\boldsymbol{u}, \boldsymbol{\phi})$, $\boldsymbol{\varepsilon}^3 = \boldsymbol{\varepsilon}^3(\boldsymbol{u}, \boldsymbol{\phi})$, and $\hat{\boldsymbol{\varepsilon}}_b^0 = \boldsymbol{\varepsilon}_b^0(\hat{\boldsymbol{u}}, \hat{\boldsymbol{\phi}})$, $\hat{\boldsymbol{\varepsilon}}_s^0 = \boldsymbol{\varepsilon}_s^0(\hat{\boldsymbol{u}}, \hat{\boldsymbol{\phi}})$, $\hat{\boldsymbol{\varepsilon}}^1 = \boldsymbol{\varepsilon}^1(\hat{\boldsymbol{u}}, \hat{\boldsymbol{\phi}})$, $\hat{\boldsymbol{\varepsilon}}^2 = \boldsymbol{\varepsilon}^2(\hat{\boldsymbol{u}}, \hat{\boldsymbol{\phi}})$, $\hat{\boldsymbol{\varepsilon}}^3 = \boldsymbol{\varepsilon}^3(\hat{\boldsymbol{u}}, \hat{\boldsymbol{\phi}})$,

$$l(\hat{\boldsymbol{u}}, \hat{\boldsymbol{\phi}}) = \int_\Omega \boldsymbol{f} \cdot \hat{\boldsymbol{u}} d\Omega + \int_{\Gamma_{N_1}} \boldsymbol{F} \cdot \hat{\boldsymbol{u}}\, d\Gamma + \int_{\Gamma_{N_2}} \boldsymbol{M} \cdot \hat{\boldsymbol{\phi}} d\Gamma. \tag{5.19}$$

with Γ_{N_1} and Γ_{N_2} denoting the natural boundaries where force and moment are applied, respectively.

The variational form of the coupling diffusion Equation (2.10) to calculate the nonlocal equivalent strain is similar to that of a boundary value problem for solids which is provided in Equation (2.33~2.35). The weak forms are discretized and numerically implemented by using isogeometric analysis with the NURBS basis function as described in Chapter 4.2.2.

5.3 Numerical examples

Herein, a numerical investigation of a thick plate of length $L = 2000\,mm$, width $W = 500\,mm$, and thickness $h = 100\,mm$ is presented. The plate is simply supported and subjected to line load along its middle section as illustrated in Figure 17. This example is studied in detail in Section 5 of Publication 4 which includes other benchmarks and examples as well, *e.g.*, a notched FG panel under tension and an FG L-shaped plated subjected to bending load. For the verification of the proposed formulations, convergence studies are conducted within a variety of mesh sizes for different geometries, boundary, and loading conditions. The results of the plate damage model are validated by comparing to experimental data and outcomings of existing approaches (see Subsections 5.1, 5.2, 5.3 of Publication 4) and commercial software, *e.g.* the Abaqus concrete damaged plasticity model.

First, the rectangular plate is tested with a single material whose properties are described in Table 3.

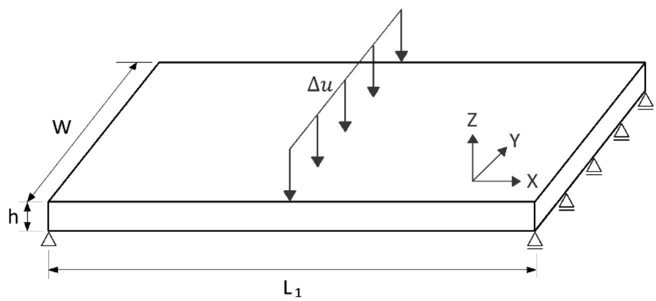

Figure 17. Functionally graded plates within different material configurations (Publication 4, Figure 12)

Table 3. Material properties of the rectangular plate in bending.

Property	Description	Value
E	Modulus of elasticity	25.85 GPa
υ	Poisson's ratio	0.18
f_t	Tensile strength	2.7 MPa

l_c	Nonlocal damage interaction parameter	$24\ \mathrm{mm}$
G_F	Fracture energy	$95\ \mathrm{N/m}$
k	Compressive/tensile strength	10

The numerical model of the plate is constructed based on the weak form in Equation (5.17) and approximated by using IGA with third-order basis functions for both the displacement, rotation, and nonlocal equivalent strain fields. The damage evolution in the plate is depicted in Figure 18 at different stages of the loading process. For comparison, a two-dimensional beam which is a cross-section in the XZ-plane of the plate is modeled with solid elements (cf. Publication 1). The damage profile of the reference beam is plotted in Figure 18f.

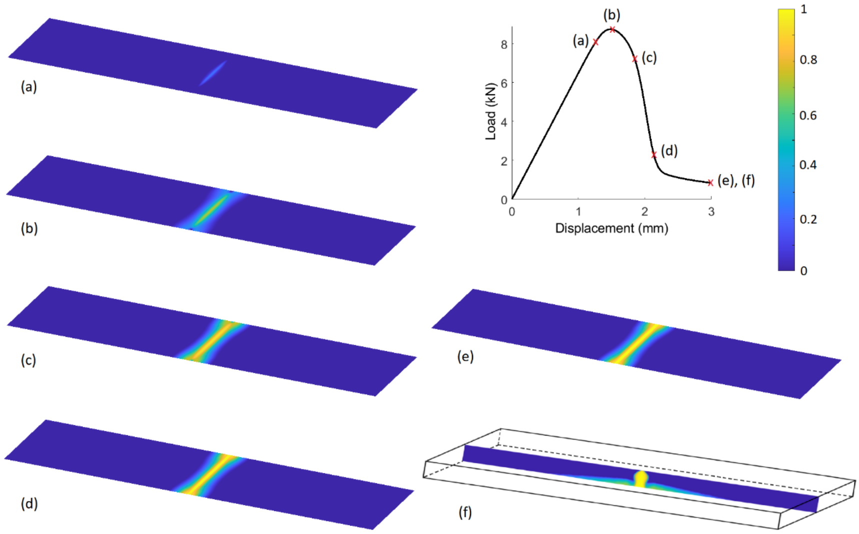

Figure 18. Damage propagation at various loading steps: (a) $\Delta u = 1.2\ mm$, (b) $\Delta u = 1.5\ mm$, (c) $\Delta u = 1.8\ mm$, (d) $\Delta u = 2.1\ mm$, (e) $\Delta u = 3.0\ mm$, (f) $\Delta u = 3.0\ mm$ with the 2D reference beam model) (Publication 4, Figure 15)

Next, a parametric study for functionally graded plates with the same geometry as the one in Figure 17 is conducted within four bi-material configurations, namely FGM-N1, FGM-N2, FGM-S1, and FGM-S2. The arrangements of the four FG plates follow Figures 16b, 16d, 16d, and 16e, respectively, where the darker shade represents material 1 and the lighter shade represents material 2. Volume fractions of the two materials along the plate thickness direction follow the exponential rules in Equations (5.1) and (5.2). Properties of the bi-material system are listed in Table 4 and corresponding properties of the mixture are calculated by the rule in Equation (5.3).

Table 4. Material properties of the functionally graded plate in bending.

Property	Description	Value	
		Material 1	Material 2
E	Modulus of elasticity	$25.85\ \mathrm{GPa}$	$12.925\ \mathrm{GPa}$
υ	Poisson's ratio	0.18	0.2
f_t	Tensile strength	$2.7\ \mathrm{MPa}$	$1.35\ \mathrm{MPa}$
l_c	Nonlocal damage interaction parameter	$24\ \mathrm{mm}$	$24\ \mathrm{mm}$
G_F	Fracture energy	$95\ \mathrm{N/m}$	$47.5\ \mathrm{N/m}$
k	Compressive/tensile strength	10	10

Figure 19 depicts the structural responses for a range of the volume fraction exponential coefficient $n = 0.2 \sim 5$. The results indicate that the material gradient profiles have significant influences on the structural behaviors of the plates. For example, in the FGM-N2 pattern, by increasing the volume fraction exponent n, the plate contains higher proportions of material 1 which is chosen to be stronger than material 2 (since the volume fraction V_1 in Equation (5.1) is always equal or smaller than unity). Specifically, higher values of n lead to more concentration of material 1 on the bottom surface of the plate bearing high tensile stress values in bending. As a result, the plate is stiffer and can endure greater loads before failure. On the other hand, FGM-N1, in which the material is arranged in the opposite manner to FGM-N2, appears to be much weaker. The symmetric material arrangement FGM-S1 follows the same trend as FGM-N2. In FGM-S1, the bottom area is majorly made of material 1, as in FGM-N2, and the placement of the stronger material on the surface subjected to high tensile stress values enables the plate to have higher endurance. Compared to the configuration FGM-S2, where material 1 is set to concentrate in the middle zone of the plate, the sandwich material pattern FGM-S1 suits much better for bending (e.g., for $n = 1$, the loading capability of FGM-S1 is $7.7\ kN$, whereas FGM-S2 only reaches $5.4\ kN$, although the two configurations have the same weight).

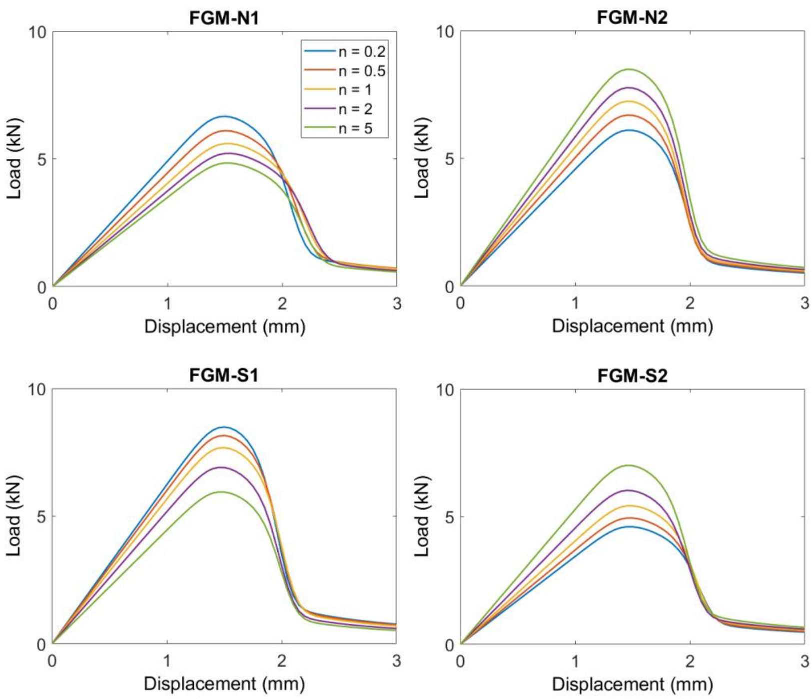

Figure 19. Force-displacement responses of FG plates subjected to bending load with various volume fraction coefficients (Publication 4, Figure 20)

6. Conclusions and recommendations for future works

6.1 Conclusions

This research is dedicated to studying an improved version of continuum damage models. Fundamental and crucial features are analyzed and developed to enhance the accuracy, stability, and applicability of the damage model. The main contents and findings of this study, via the four Publications are presented as follows:

Publication 1: The nonlocal interactions of the intrinsic micro defects in quasi-brittle materials are addressed. A novel evolving gradient parameter is formulated to describe the nonlocal interactions in the damage micro process in a more appropriate manner. The intensity and orientation of the microscopic nonlocal interaction zones are characterized and controlled by the stress and strain states. A convenient law to calculate the scalar equivalent strain is proposed based on the bi-energy norm concept, comprising both contributions of the tensile and compressive strains. A formula to determine the model parameters, *e.g.*, the softening rate and the nonlocal interaction length, from the physical fracture energy is derived. That results in a correct capturing of damage zones surrounding notch tips and shear bands under compressive loads, where the conventional approaches struggle. A stress smoothing process is introduced to tackle the stress oscillation caused by the mismatch of the coupling fields. That enables the damage model to be employed within low-order finite elements, which significantly reduces the computational resource requirements. The proposed features have been demonstrated through a variety of numerical experiments as well as in different applications in Publications 2, 3, and 4.

Publication 2: The damage model is adapted so that it can be utilized for the simulation of heterogeneous materials. A methodology to virtually generate material domains with spatially random and correlated properties, *e.g.*, Young's modulus and tensile strength, is employed. Random specimens with different geometries and loading configurations are simulated and the outcomings are statically analyzed to find out the influence of uncertain inputs on the output values. The results reveal, in general, that the tensile strength variability contributes to the damage behaviors substantially more (up to 4 times) than the elasticity modulus; and material heterogeneities reduce the loading capability of structures. The good agreement between the numerical and experimental results suggests that this approach can offer a relatively inexpensive alternative to replicate the expensive laboratory tests.

Publication 3: The damage model is developed to deal with quasi-brittle materials containing microarchitectures. The governing equation of the displacement field adopts a simplified version of Mindlin's theory, where the material internal structures are effectively homogenized by the second strain gradient formulations with corresponding length scale parameters. Hence, the microstructural materials can be treated as homogeneous media in the damage modeling process. This approach vastly reduces the geometric complexity of the classical models, which require explicit modeling of internal structures.

Numerically, this damage model is implemented by using the framework of isogeometric analysis. The NURBS basis functions of third-order are exploited to satisfy the C^2-continuity across element boundaries required by the second strain gradient theory. By the way, this damage model has been developed as a single-scale approach, enabling a simple application and integration to current finite element packages. Compared to the damage model proposed by Putar *et al.* (2017), this approach does not demand proprietary elements which include more degrees of freedom for the derivatives at the vertices and the middle of element edges; as well as a multiscale simulation. In general, this second strain gradient damage model takes into account both the nonlocality induced by the interactions of micro defects which are the nature of quasi-brittle damage; and the size effects caused by the manufactured microarchitectures.

Publication 4: The evolving damage model is tailored to the functionally graded plates of third-order shear deformation theory. The concept of a physical neutral surface is adopted to increase the simulation accuracy since the neutral surface is significantly shifted from the geometric middle plane in cases of inhomogeneous materials. The coupling governing equations of displacement and nonlocal equivalent strain that drive the damage propagation are defined on the neutral surface. For each plate cross-section, stiffness coefficients can be computed by analytical integration in contrast to numerical integration over the plate thickness, as in other approaches. That helps to reduce computational effort and maintain the simplicity of the dimensional reduction model. Regarding the implementations, plates are intensively tested within homogeneous and four graded material configurations with different geometries, in comparison to results from experiments, other numerical approaches, as well as a predefined concrete damaged plasticity model in Abaqus. The results demonstrate the validity, accuracy, and applicability of the proposed formulations.

6.2 Recommendations for future works

While boasting the improved features and implementations in a wide range of applications, the study presented in this dissertation has certain shortcomings, which are the subject of interest for further research:

- The damage model is limited to certain quasi-brittle materials and tensile-dominated loading schemes. Although it can be adjusted to tackle various brittleness by altering the compressive/tensile strength ratio, ductile damage is out of scope since it requires a regime of plastic deformation. As well, modeling of highly confined quasi-brittle substances like deeply underground rocks is not applicable.
- The damage model is limited to quasi-static simulations.
- Concerning the numerical implementation aspect, the damage model is developed by using an in-house MATLAB finite element package, which is convenient for the algorithm testing process but is unfavorable in terms of calculation speed and usage of computational resources. That refrains the damage model from practical/engineering large-scale applications.
- The damage model introduces certain intuitive parameters for model calibration from experimental measurements. However, in this work, they are obtained by trial-and-error method or from the author's experience, thanks to the lack of laboratory testing.

For future research, it is worth incorporating a plasticity model into the current damage model, which will open the door to the modeling of a large number of materials, under a wide range of loading conditions, e.g., rocks subjected to triaxial compression, more accurately and practically. Next, a high-performance finite element package developed in Fortran, C++, or Python is necessary as it can greatly save computational time, offer more computing features and enable quick development of algorithms and applications. Lastly, establishing more collaboration with groups that are specialized in experimental studies is admirable.

References

Akarapu S., Zbib H. M. (2006). Numerical analysis of plane cracks in strain gradient elastic materials. International Journal of Fracture, 141, 403-430.

Alfarah B., Lopez-Almansa F., Oller S. (2017). New methodology for calculating damage variables evolution in Plastic Damage Model for RC structures. Engineering structures, 132, 70-86.

Aliha, M. R. M., Heidari-rarani, M., Shokrieh M. M. Ayatollahi, M. R. (2012). Experimental determination of tensile strength and K (IC) of polymer concretes using semi-circular bend (SCB) specimens. Structural Engineering and Mechanics, 43, 823-833.

Altan B., Aifanis E. (1997). On some aspects in the special theory of gradient elasticity. Journal of the Mechanical Behavior of Materials, 8, 231-282.

Ambati M., Gerasimov T., De Lorenzis L. (2014). A review on phase-field models and a new fast hybrid formulation. Computational Mechanics, 55(2), 483-405.

Ambati M., Gerasimov T., De Lorenzis L. (2015). Phase-field modeling of ductile fracture. Computational Mechanics, 55(5), 1017-1040.

Amiri F., Millan D., Shen Y., Rabczuk T., Arroyo M. (2014). Phase-field modeling of fracture in linear thin shells. Theoretical and Applied Fracture Mechanics, 69, 102-109.

Amor H., Marigo J. -J., Maurini C. (2009). Regularized formulation of the variational brittle fracture with unilateral contact: Numerical experiments. Journal of the Physics and Mechanics of Solids, 57 1209-1229.

Andreaus U., Dell'Isola F., Giorgio I., Placidi L., Lekszycki T., Rizzi N. L. (2016). Numerical simulations of classical problems in two-dimensional (non) linear second gradient elasticity. International Journal of Engineering Science, 108, 34-50.

Askes H., Aifantis E.C. (2011). Gradient elasticity in static and dynamics: An overview of formulations, length scale identification procedures, finite element implementations and new results. International Journal of Solids and Structures, 48, 1962-1990.

Balobanov V., Kiendl J., Khakalo S., Niiranen J. (2019). Kirchhoff-Love shells within strain gradient elasticity: Weak and strong formulation and an H3-conforming isogeometric implementation. Computer Methods in Applied Mechanics and Engineering, 344, 837-857.

Balobanov V., Niiranen J. (2018). Locking-free variational formulations and isogeometric analysis for the Timoshenko beam models of strain gradient and classical elasticity. Computer Methods in Applied Mechanics and Engineering, 339, 137-159.

Bažant Z. P. (1991). Why continuum damage is nonlocal: Micromechanical arguments. Journal of Engineering Mechanics, 117, 1070-1087.

Bažant Z. P. (1994). Nonlocal damage theory based on micromechanics of crack interaction. Journal of Engineering Mechanics, 120, 1070-1087.

Bažant Z. P., Pjiaudier-Carbot G. (1989). Measurement of characteristic length of nonlocal continuum. Journal of Engineering Mechanics, 115, 755-767.

Bazilevs J. Y., Pigazzini M. S., Ellison A., Kim H. (2018). A new multi-layer approach for progressive damage simulation in composite laminates based on isogeometric

analysis and Kirchhoff-Love shells. Part I: basic theory and modeling of delamination and transverse shear. Computational Mechanics, 62, 563-585.
Bouazza M., Tounsi A., Adda-Bedia E. A., Megueni A. (2010). Thermal elastic stability analysis of functionally graded plates: and analytical approach. Computational Material Science, 49, 865-870.
Bourdin B., Francfort G. A., Marigo J. -J. (2000). Numerical experiments in revisited brittle fracture. Journal of the Mechanics and Physics of Solids, 48, 797-826.
Bui Q. T., Nguyen H. A. T., Doan H. D., Nguyen D. D., Hirose S. (2016). Numerical failure simulation of quasi-brittle materials using a second-order implicit gradient damage theory. The 4th International Conference on Engineering Mechanics and Automation, Vietnam.
Bui Q. T., Nguyen H. A. T., Hirose S. (2017). Failure modeling of quasi-brittle materials by low-order finite element and stress-based gradient damage model. Proceeding of the 6th Biot Conference on Porous Mechanics, France, https://doi.org/10.1061/9780784480779.221, 1789-1896.
Bui Q. V., Lani. F. (2011). Non-local implicit gradient damage models with low-order finite element. International Journal of Numerical Methods in Biomedical Engineering, 27, 962-976.
Caro S., Castillo D., Darabi M. K., Masad E. (2017). Influence of different sources of microstructural heterogeneity on the degradation of asphalt mixtures. International Journal of Pavement Engineering, 19, 9-23.
Carpiuc-Prisacari A., Jailin C., Poncelet M., Kazymyrenko K., Leclerc H., Hild F. (2019). Experimental database of mixed-mode crack propagation tests performed on concrete specimens with a hexapod and full-field measurements Part II: interactive loading. Cement and Concrete Research, 125, 105867.
Castillo D., Nguyen H. A. T. Niiranen J. (2021). Spatially random modulus and tensile strength: contribution to variability of strain, damage, and fracture in concrete. International Journal of Damage Mechanics, Article in Press.
Chen J., Wang H., Dan H. & Xie Y. (2018a). Random modeling of three-dimensional heterogeneous microstructure of asphalt concrete for mechanical analysis. Journal of Engineering Mechanics, 144, 04018083.
Chen Q., Zhu H., Ju J., W. Jiang, Z. Yan Z., Li H. (2018b). Stochastic micromechanical predictions for the effective properties of concrete considering the interfacial transition zone effects. International Journal of Damage Mechanics, 27, 1252-1271.
Cicekli U., Voyiadjis G., Al-rub R. A. (2007). A plasticity and anisotropic damage model for plain concrete. International Journal of Plasticity, 23, 1874-1900.
Comi C., Perego U., (2001). Fracture energy based bi-dissipative damage model for concrete. International Journal of Solids and Structures, 38, 6427-6454.
Comi C., Mariani S. (2007). Extended finite element simulation of quasi-brittle fracture in functionally graded materials. Computer Methods in Applied Mechanics and Engineering, 196, 4013-4026.
Cuomo M., Loredana C., Leopoldo G. (2014). A variational model based on isogeometric interpolation for the analysis of cracked bodies. International Journal of Engineering Science, 80, 173-188.
De Angelo M., Spagnuolo M., D'Annibale F., Pfaff A., Hoschke K., Misra A., Dupuy C., Peyre P., Dirrenberger J., Pawlikowski M. (2019). The macroscopic behavior of pantographic sheets depends mainly on their microstructure: experimental evidence and qualitative analysis of damage in metallic specimens. Continuum Mechanics and Thermodynamics, 31(1), 1181-1203.

de Borst R., Verhoosel C. V. (2016). Gradient damage vs phase-filed approaches for fractures: Similarities and differences. Computer Methods in Applied Mechanics and Engineering, 312, 78-94.

de Vree J. H. P., Brekelmans W. A. M., van Gils M. A. (1995). Comparison of non-local approaches in continuum mechanics. Computers and Structures, 55, 581-588.

dell'Isola F., Seppecher P., Spagnuolo M., Barchiesi B., Hild F., Lekszycki T., Giorgio I., Placidi L., Andreaus U., Cuomo M., Eugster S. R., Hoschke K., Langkemper R., Turco E., Sarikaya R., Misra Aviral., De Angelo M., Annibale F. D., Bouterf A., Pinelli X., Misra Anil, Desmorat B., Pawlikowski M., Dupuy C., Scerrato D., Peyre P., Laudato M., Manzari., Göransson P., Hesch C., Hesch S., Franciosi P., Dirrenberger J., Maurin F., Vangelatos Z., Grigoropoulos c. P., Melissinaki V., Farsari M., Muller W., Abali B. E., Liebold C., Ganzosch G., Harrison P., Drobnicki R., Igumnov L., Alzahrani F., Hayat T. (2019). Advances in Pantographic Structures: Design, Manufacturing, Models, Experiments and Image Analyses. Continuum Mechanics and Thermodynamics, 31(4), 1231-1282.

Do V. T., Doan H. D., Nguyen D. D., Bui Q. T. (2017). Phase-field thermal buckling analysis of cracked functionally graded composite plates considering neutral surface. Composite Structures, 182, 542-548.

Doan H. D., Bui Q. T., Do T. V., Nguyen D. D. (2017). A rate-dependent hybrid phase-field model for dynamics crack propagation. Journal of Applied Physics, 122, 102-115.

Doan H. D., Bui Q. T., Nguyen D. D., Fushinobu K. (2016). Hybrid phase field simulation of dynamic crack branching in functionally graded glass-filled epoxy. Composite Part B: Engineering, 99, 266-276.

Dong Y., Su C., Qiao P., Sun L. Z. (2018). Microstructural damage evolution and its effect on fracture behavior of concrete subjected to freeze-thaw cycles. International Journal of Damage Mechanics, 27, 1272-1288.

Dragon A., Halm D., Desoyer Th. (2000). Anisotropic damage in quasi-brittle solids: modeling, computational issues and applications. Computer Methods in Applied Mechanics and Engineering, 183, 331-352.

Dragon A., Mróz Z. (1979). A continuum damage model for plastic-brittle behavior of rock and concrete. International Journal of Engineering Science, 17, 121-137.

Duda P. F., Ciarbonetti A., Sánchez J. P., Huespe E. A. (2015). A phase-field/gradient damage model for brittle fracture in elastic-plastic solids. International Journal of Plasticity, 65, 269-296.

Eliáš J., Vorechovsky M., Skocek J., Bažant Z. P. (2015). Stochastic discrete meso-scale simulations of concrete fracture: Comparison to experimental data. Engineering Fracture Mechanics, 135, 1–16.

El-Kadi A. I., Williams S.A. (2000). Generating Two-Dimensional Fields of Autocorrelated, Normally Distributed Parameters by the Matrix Decomposition Technique. Ground Water, 38, 530-532.

Erdogan F., Wu B. H. (1996). Crack problem in FGM layers under thermal stresses. Journal of Thermal Stresses, 19, 237-265.

Ferte G., Massin P., Moes N. (2016), 3D crack propagation with cohesive elements in the extended finite element method. Computer Methods in Applied Mechanics and Engineering, 300, 347–374.

Fish J., Belytschko T. (2007). A first course in Finite Elements. Wiley, ISBN: 978-0-470-03580-1

Francfort G. A., Marigo J-. J. (1998). Revisiting brittle fractures as an energy minimization problem. Journal of the Mechanics and Physics of Solids, 46, 1319-1342.

Geers M. G. D., de Borst R., Brekelman W. A. M., Peerlings R. J. H. (1998). Strain-based transient-gradient damage model for failure analyses. Computer Methods in Applied Mechanics and Engineering, 160, 133-153.

Geers M. G. D., Kouznetsova V. G., Brekelmans W. A. M. (2010). Multi-scale computational homogenization: trends and challenges. Journal of Computational and Applied Mathematics, 234(7), 2175-2182.

Geuzaine C., Remacle J. (2009). Gmsh: A three-dimensional finite element mesh generator with built-in pre- and post-processing facilities. International Journal for Numerical Methods in Engineering, 79, 1309-1331.

Giry C., Dufort F., Massart J. T. (2011). Stress-based non-local damage model. International Journal of Solids and Structures, 48, 3431-3443.

Grassl P., Jirásek M. (2006). Damage-plastic model for concrete failure. International Journal of Solids and Structures, 43, 7166-7196.

Grassl P., Lundgren K., Gylltoft K. (2002). Concrete in compression, a plasticity theory with a novel hardening law. International Journal of Solids and Structures, 39, 5205-5223.

Guillén-Hernández T., Reinoso J., Paggi M. (2020). Phase field model for fracture analysis of functionally graded power-based shell structures. Mechanics of Advanced Materials and Structures. https://doi.org/10.1080/15376494.2020.1751354

Guo L. P., Carpinteri A., Roncella R., Spagnoli A., Sun W., Vantadori S. (2009). Fatigue damage of high-performance concrete through a 2D mesoscopic lattice model. Computational Materials Science, 44, 1098–1106.

Han T. S., Zhang X., Kim J. S., Chung S. Y., Lim J. H., Linder C. (2018). Area of lineal-path function for describing the pore microstructures of cement paste and their relations to the mechanical properties simulated from micro-CT microstructures. Cement and Concrete Composites, 89, 1-17.

Heidari-Rarani M., Bashandeh-Khodaei-Naeini K. (2018). Micromechanics based damage model for predicting compression behavior of polymer concretes. Mechanics of Materials, 117, 126-136.

Heidari-Rarani M., Sayedain M. (2019). Finite element modeling strategies for 2D and 3D delamination propagation in composite DCB specimens using VCCT, CZM and XFEM approaches. Theoretical and Applied Fracture Mechanics, 103, 102246.

Hillerborg A., Modeer M., Peterson P. E. (1976). Analysis of crack formulation and crack growth in the concrete by means of fracture mechanics and finite elements. Cement and Concrete Research, 6, 773-782.

Hirshikesh, Natarajan S., Annabattula R. K., Martinez-Paneda E. (2019). Phase field modeling of crack propagation in functionally graded materials. Composite Part B: Engineering, 169, 239-248.

Hordijk D. A. (1974). Local approach to fatigue of concrete. Technisch Universiteit Delft, Ph.D. thesis, ISBN 90-9004519-8.

Hosseini S., Remmers J. J. C., de Borst R. (2014). The incorporation of gradient damage models in shell elements. International Journal of Numerical Methods in Engineering, 98, 391-398.

Hughes T., Cottrell J., Bazilevs Y. (2005). Isogeometric analysis: CAD, finite elements, nurbs, exact geometry and mesh refinement. Computer Methods in Applied Mechanics and Engineering, 194, 4135-4195.

Ibrahimbegovic A., Marcovic D., Gatuingt F. (2003). Constitutive model of coupled damage-plasticity and its finite element implementation. Revue Européenne des Eléments Fins, 12, 381-405.

Irwin G. R. (1957). Analysis of stresses and strains near the end of a crack traversing a plate. Journal of Applied Mechanics, 24, 361-364.

Janiszewski M., Shen B., Rinne M. (2019). Simulation of the interactions between hydraulic and natural fractures using a fracture mechanics approach. Journal of Rock Mechanics and Geotechnical Engineering, 11, 1138-1150.

Javaheri R., Elasmi M. R. (2002). Thermal buckling of functionally graded plates based on higher order theory. Journal of Thermal Stresses, 25, 603-625.

Jefferson A., Mihai I., Tenchev R., Alnass W., Cole G., Lyons P. (2016). A Plastic-damage-contact constitutive model for concrete with smoothed evolution functions. Computers and Structures, 169, 40-56.

Jirásek M. (2008). Nonlocal models for damage and fracture: comparison of approaches. International Journal of Solids and Structures, 35, 4133-4145.

Jirásek M. (2017). Nonlocal damage models for damage and fractures: comparison of approaches. International Journal of Solids Structures, 132, 70-86.

Jirásek M., Bauer M. (2012). Numerical aspects of the crack band approach. Computers and Structures, 110-111, 60-78.

Jirásek M., Rolshoven S., Grassl P. (2004). Size effects on the fracture energy induced by nonlocality. International Journal of Numerical and Analytical Methods in Geomechanics, 28, 653-670.

Kapuria S., Bhattacharrya M., Kumar A. N. (2008). Bending and free vibration response of layered functionally graded beams: a theoretical model and its experimental validation. Composite Structures, 82, 390-402.

Khakalo S., Balobanov V., Niiranen J. (2018). Modeling size-dependent bending, buckling and vibrations of 2D triangular lattices by strain gradient elasticity models: application to sandwich beams and auxetics. International Journal of Engineering Science, 127, 33-52.

Khakalo S., Niiranen J. (2017). Isogeometric analysis of higher-order gradient elasticity by user elements of a commercial finite element software. Computer-Aided Design, 81, 154-169.

Kiendl J., Ambati M., De Lorenzis L., Gomez H., Reali A. (2016). Phase-field description of brittle fractures in plates and shells. Computer Methods in Applied Mechanics and Engineering, 312, 374-394.

Koksal O. H., Karakoc C. (1999). An anisotropic damage model for concrete. Materials and Structures, 32, 611-617.

Kuhl E., Ramm E., de Borst R. (2000). An anisotropic gradient damage model for quasi-brittle materials. Computer Methods in Applied Mechanics and Engineering, 183, 87-103.

Kurumatani M., Terada K., Kato J., Kyoya T., Kashiyama K. (2016). An isotropic damage model based on fracture mechanics for concrete. Engineering Fracture Mechanics, 155, 49-66.

Laudato M., Manzari L, Giorgio I., Spagnuolo M., Göransson P. (2021). Dynamics of pantographic sheets around the clamping region: experimental and numerical analysis. Mathematics and Mechanics of Solids, https://doi.org/10.1177/1081286521992646.

Le L. A., Nguyen G. D., Bui H. H., Sheikh A. H., Kotousov A. (2019). Incorporation of micro-cracking and fibre bridging mechanisms in constitutive modelling of fibre reinforced concrete. Journal of the Mechanics and Physics of Solids, 133, 103732.

Lee Y. H., Bae S. I., Kim J. H. (2016), Thermal buckling behavior of functionally graded plates based on neutral surface. Composite Structures, 137, 208-214.

Lesicar T., Tonkovic Z., Soric J. (2014). A second-order two-scale homogenization procedure using C-1 macrolevel discretization. Computational Mechanics, 54(2), 425-441.

Li T., Marigo J. -J., Guilbaud D., Potapov S. (2016). Gradient damage modeling of brittle fracture in an explicit dynamics contest. International Journal of Numerical Methods in Engineering, 108(12), 1381-1405.

Lian C., Zhuge Y., Beecham S. (2011). The relationship between porosity and strength for porous concrete. Construction and Building Materials, 25, 4294-4298.

Massart T. J., Peerlings R. J. H., Geers M. G. D. (2007). An enhanced multi-scale approach for masonry wall computation with localization of damage. International Journal of Numerical Methods in Engineering, 69(5), 2175-2182.

Mazars J., Pjiaudier-Carbot G. (1989). Continuum damage theory – application to concrete. Journal of Engineering Mechanics, 115, 345-365.

Mazars J., Pjiaudier-Carbot G. (1996). From damage to fracture mechanics and conversely: a combined approach. International Journal of Solids and Structures, 33, 3327-3342.

Menétrey P., Willam K. (1995). A triaxial failure criterion for concrete and its generalization. ACI Structural Journal, 92, 311-318.

Meschke G., Dumstorff P. (2007). Energy-based modeling of cohesive and cohesionless crack via X-FEM. Computer Methods in Applied Mechanics and Engineering, 196, 2338-2357.

Miehe C., Welschinger F., Hofacker M. (2010). Thermodynamically consistent phase-field models of fractures: Variational principles and multi-field FE implementations. International Journal of Numerical Methods in Engineering, 83, 1273-1311.

Mikkola M., Schnobrich W. C. (1970). Material behavior characteristics for reinforced concrete shells stressed beyond the elastic range. Technical Report, 367. University of Illinois, Urbana-Champaign.

Mindlin R. (1964). Micro-structure in linear elasticity. Archive for Rational Mechanics and Analysis, 16(1), 51-78.

Moes N., DolBow J., Belytschko T. (1999). A finite element method for crack growth without remeshing. International Journal of Numerical Methods in Engineering, 46(1), 131–150.

Moes N., DolBow J., Belytschko T. (2002) Extended finite element method for cohesive crack growth. Engineering Fracture Mechanics, 69(7), 813-833.

Mühlich U., Zybell L., Hütter G., Kuna M. (2013). A first order strain gradient damage model for simulating quasi-brittle failure in porous elastic solids. Archives of Applied Mechanics, 83, 955-967.

Negi A., Kumar S., Poh L.H. (2020). A localizing gradient damage enhancement with micromorphic stress-based anisotropic nonlocal interactions. International Journal for Numerical Methods in Engineering, 121, 4403-4027.

Nguyen D. G. (2011). A damage model with evolving nonlocal interactions. International Journal of Solids and Structures, 48, 1544-1559.

Nguyen D. G., Houlsby T.G. (2007). Non-local damage modelling of concrete: a procedure for the determination of model parameters. International Journal of Numerical and Analytical Methods in Geomechanics, 31, 867-891.

Nguyen H. A. T. Niiranen J. (2021). Nonlocal continuum damage modeling for functionally graded plates of third-order shear deformation theory. Thin-walled Structures, Article in Press.

Nguyen H. A. T., Bui Q. T., Hirose S. (2018) Smoothing gradient damage model with evolving anisotropic nonlocal interactions tailored to low-order finite elements. Computer Methods in Applied Mechanics and Engineering, 328, 498-541.

Nguyen H. A. T., Niiranen J. (2020). A second strain gradient damage model with a numerical implementation for quasi-brittle materials with micro-architectures. Math. Mech. Solids, 25(3), 515-546.

Nguyen V. P., Anitescu C., Bordas S. P. A, Rabczuk T. (2015). Isogeometric analysis: An overview and computer implementation aspects. Mathematics and Computers in Simulation, 117, 89-116.

Nguyen V. P., Stroeven M., Sluys L. J. (2012). An enhanced continuous-discontinuous multiscale method for modeling mode-I failure in random heterogeneous quasi-brittle materials. Engineering Fracture Mechanics, 79, 78-102.

Niiranen J., Khakalo S., Balobanov V., Niemi A. H. (2016). Variational formulation and isogeometric analysis for fourth-order boundary value problems of gradient-elastic bar and plane strain/stress problems. Computer Methods in Applied Mechanics and Engineering, 308, 182-211.

Niiranen J., Kiendl J., Niemi A. H., Reali A. (2017). Isogeometric analysis for sixth-order boundary value problems of gradient-elastic Kirchhoff plates. Computer Methods in Applied Mechanics and Engineering, 316, 328-348.

Nooru-Mohamed, M. B. (1992). Mixed-Mode Fracture of Concrete. Delft University of Technology, the Netherland. Ph.D. thesis.

Papanikolaou V., Kappos A. (2007). Confinement-sensitive plasticity constitutive model for concrete in triaxial compression. International Journal of Solids and Structures, 44, 7021-7048.

Park K., Paulino G. H. (2013). Cohesive zone models: A critical review of traction-separation relationships across fracture surfaces. Applied Mechanics Reviews, 64(6), 060802-20.

Peerlings R. J. H., de Borst R., Brekelman W. A. M., de Vree J. H. P. (1996). Gradient enhanced damage for quasi-brittle materials. International Journal of Numerical Methods in Engineering, 39, 937-953.

Peerlings R. J. H., Geers M. G. D., de Borst R., Brekelman W. A. M. (2001). A critical comparison of nonlocal and gradient-enhanced softening continua. International Journal of Solids and Structures, 38, 7723-7746.

Peerlings R. J. H., Massart J. T., Geers M. G. D. (2004). A thermodynamically motivated implicit gradient damage framework and its application to brick masonry cracking. Computer Methods in Applied Mechanics and Engineering, 193, 3403-3417.

Pigazzini M. S., Bazilevs J. Y., Ellison A., Kim H. (2018). A new multi-layer approach for progressive damage simulation in composite laminates based on isogeometric analysis and Kirchhoff-Love shells. Part II: impact modeling. Computational Mechanics, 62 (2018) 587-601.

Pigazzini M. S., Kamensky D., van Iersel D. A. P., Alaydin M. D., Remmers J. J. C., Bazilevs Y. (2019). Gradient-enhanced damage modeling in Kirchhoff-Love shells: Application to isogeometric analysis of composite laminates. Computer Methods in Applied Mechanics and Engineering, 346, 152-179.

Pijaudier-Carbot G., Haidar K., Dubé J. F. (2004). Nonlocal damage model with evolving internal length. International Journal of Numerical and Analytical Methods in Geomechanics, 28, 633-652.

Placidi L. (2015). A variational approach for a nonlinear 1-dimensional second gradient continuum damage model. Continuum Mechanics and Thermodynamics, 27, 623-638.

Placidi L., Barchiesi E., Misra A. (2018a). A strain gradient variational approach to damage: A comparison with damage gradient models and numerical results. Mathematics and Mechanics of Complex Systems, 6(2), 77-100.

Placidi L., Barchiesi E., Misra A. (2018b). Two-dimensional strain gradient damage modeling: a variational approach. Zeitschrift für angewandte Mathematik und Physik, 69, 56.

Placidi L., Barchiesi E., Misra A., Andreaus U. (2020). Variational methods in continuum damage and fracture mechanics. Encyclopedia of Continuum Mechanics. Eds. H. Altenbach, A. Öchsner, https://doi.org/10.1007/978-3-662-53605-6_199-1.

Poh L. H., Sun G. (2017). Localization gradient damage model with decreasing interactions. International Journal of Numerical Methods in Engineering, 110, 503-522.

Pradhan K. K., Chakraverty S. (2013). Free vibration of Euler and Timoshenko functionally graded beams by Rayleigh-Ritz method. Composites Part B: Engineering, 51, 175-84.

Prakash T., Singha M. K., Gahapathi M. (2009). Influence of neutral surface position on the nonlinear stability behavior of functionally graded plates. Computational Mechanics, 43, 341-350.

Putar F., Soric J., Lesicar T., Tonkovic Z. (2017). Damage modeling employing strain gradient continuum theory. International Journal of Solids and Structures, 120, 171-185.

Qin X., Gu C., Shao C., Fu X., Vallejo L., CHen Y. (2020). Numerical analysis of fracturing behavior in fully-graded concrete with oversized aggregates from mesoscopic perspective. Construction and Building Materials, 253, 1-17.

Reddy J. N. (2000). Analysis of functionally graded plates. International Journal of Numerical Methods in Engineering, 47, 663-684.

Reddy J. N. (1990). A general non-linear third-order theory of plates with moderate thickness. International Journal of Non-linear Mechanics, 25(6), 677-686.

Ren H. L., Zhuang X. Y., Atitescu C., Rabczuk T. (2019). An explicit phase-field method for brittle dynamics fracture, Computers and Structures, 217, 45-56.

Resende L. (1987). A damage mechanics constitutive theory for the inelastic behavior of concrete. Computer Methods in Applied Mechanics and Engineering, 60, 57-93.

Rizzi E. (1994). Fracture-energy-based regularization of a scale damage model. Proceeding of Ottavo Italiano di Meccanica Computazionale, Italy.

Rizzi E., Carol I., William K. (1995). Localization analysis of elastic degradation with application to scalar damage. Journal of Engineering Mechanics, 121, 541-554.

Roy D. M., Gouda G. R. (1973). Porosity-strength relation in cementitious materials with very high strength. Journal of the American Ceramic Society – Discussion and Notes, 56(10), 549-550.

Salimzadeh Z., Khalili N. (2015). A three-phase XFEM model for hydraulic fracturing with cohesive crack propagation. Computers and Geotechnics, 69, 82-92.

Sargado J. M., Keilegavlen E., Berre I., Nordbotten J.M. (2018). High-accuracy phase-field models for brittle fracture based on a new family of degradation functions. Journal of the Mechanics and Physics of Solids, 111, 458-489.

Saroukhani S., Vafadari R., Simone A. (2013). A simplified implementation of a gradient-enhanced damage model with transient length scale effects. Computational Mechanics, 51, 899-909.

Schulz U., Peters M., Bach F-W., Tegeder G. (2003). Graded coatings for thermal, wear and corrosion barriers. Material Science and Engineering: A, 362, 61-80.

Simon K. M., Chandra-Kishen, J. M. (2016). Influence of aggregate bridging on the fatigue behavior of concrete International Journal of Fatigue, 90, 200-209.

Simone A., Askes H., Peerlings R. J. H., Sluys L. J. (2003). Interpolation requirements for implicit gradient-enhanced continuum damage models. Communications in Numerical Methods in Engineering, 19, 563-572.

Simone A., Askes H., Sluys L. J. (2004). Incorrect initiation and propagation of failure in non-local and gradient-enhanced media. International Journal of Numerical Methods in Engineering, 41, 351-363.

Spagnuolo M., Yidizdag M. E., Andreaus U., Cazzani M. A. (2020). Are higher-gradient models also capable of predicting mechanical behavior in the case of wide-knit pantographic structures? Mathematics and Mechanics of Solids, 26(1), 18-29.
Su H., Banerjee J. R. (2015). Development of dynamic stiffness method for free vibration of functionally graded Timoshenko beams. Computers and Structures, 147, 107-116.
Suchorzewski J., Tejchman J., Nitka M. (2018). Discrete element method simulations of fracture in concrete under uniaxial compression based on its real internal structure. International Journal of Damage Mechanics, 27, 578-607.
Sun G., Poh L. H. (2016). Homogenization of intergranular fracture towards a transient damage model. Journal of the Mechanics and Physics of Solids, 95, 374-392.
Torabi J., Ansari R. (2020). Crack propagation in functionally graded 2D structures: A finite element phase-field study. Thin-walled Structures, 151, 106734.
Tran Q. A., Nguyen H. A. T., Niiranen J., Sołowski W. (2019). Continuum damage modelling of quasi-brittle materials by using the material point method. Proceedings of the 32nd Nordic Seminar on Computational Mechanics (NSCM 32), Oulu, Finland.
Tran Q. T., Rabczuk T., Bazilevs Y., Meschke G. (2016). A higher-order stress-based gradient-enhanced damage model based on isogeometric analysis. Computer Methods in Applied Mechanics and Engineering, 304, 584-604.
Valvo P. S. (2012). A revised virtual crack closure technique for physically consistent fracture mode partitioning. International Journal of Fracture, 173, 1-20.
Vanmarcke E. (1983). Random Fields: Analysis and Synthesis, Cambridge, MA, MIT Press.
Verhoosel C. V., Scott M. G., Hughes T. J. R., de Borst R. (2011). An isogeometric analysis approach to gradient damage models. International Journal of Numerical Methods in Engineering, 86, 115-134.
Vilppo J., Kouhia R., Hartikainen J., Kolari K., Fedoroff A., Calonius K. (2021). Anisotropic damage model for concrete and other quasi-brittle materials. International Journal of Solids and Structures, 225, 111048.
Volokoh K. Y. (2012). Characteristic length of damage localization in steel. Engineering Fracture Mechanics, 94, 85-86.
Volokoh K. Y. (2013). Characteristic length of damage localization in concrete. Mechanics Research Communications, 51, 29-31.
Voyiadjis G., Taqieddin Z., Kattan P. (2008). Anisotropic damage-plasticity model for concrete. International Journal of Plasticity, 24, 1946-1965.
Wang Y. X., Waisman H. (2016). From diffusive damage to sharp cohesive cracks: A coupled XFEM framework for failure analysis of quasi-brittle materials. Computer Methods in Applied Mechanics and Engineering, 299, 57-89.
Willam K., Warnke E. (1975). Constitutive model for the trial behaviour of concrete. In: IABSE Proceeding, Seminar on Concrete Structures Subjected to Triaxial Stresses, Bergamo, Italy, 1-30.
Winkler B. J. (2001). Traglastuntersuchungen Von Unbewehrten Und Bewehrten Betonstukturen Auf Der Grundlage Eines Objektiven Werkstoffgesetzes Fur Beton, Innsbruck University, Ph.D. thesis.
Wolff C., Richart N., Molinari J-F. (2015). A nonlocal continuum damage approach to model dynamics crack branching. International Journal of Numerical Methods in Engineering, 101(12), 933-949.
Wu C. T., Wu Y. C., Koishi M. (2015). A strain-morphed nonlocal meshfree method for the regularized particle simulation of elastic-damage induced strain localization problems. Computational Mechanics, 56, 1039-1054.

Wu J. Y., Nguyen V. P. (2018). A length scale insensitive phase-field damage model for brittle fracture. Journal of the Physics and Mechanics of Solids, 119, 20-42.

Yang Y., Misra A. (2010). Higher-order stress-strain theory for damage modeling implemented in an element-free Galerkin formulation. Computer Modeling in Engineering and Science, 64(1), 1-36.

Yang Z., Ren W., Sharma R., McDonald S., Mostafavi M., Vertyagina Y., Marrow T. J. (2017). In-situ X-ray computed tomography characterisation of 3D fracture evolution and image-based numerical homogenisation of concrete. Cement and Concrete Composites, 75.

Yilmaz O., Molinari J. F. (2017). A mesoscale fracture model for concrete. Cement and Concrete Research, 97, 84-94.

You T., Abu Al-Rub R. K., Darabi M. K., Masad E. A., Little D.N. (2012). Three-dimensional microstructural modeling of asphalt concrete using a unified viscoelastic–viscoplastic–viscodamage model. Construction and Building Materials, 28, 531–548.

Zhang, X. D., Bui Q. T. (2015). A fictitious crack XFEM with two new solution algorithms for cohesive crack growth modeling in concrete structures. Engineering Computations, 32, 473-497.

Quasi-brittle fracture – characteristic for mineral-based materials typical in construction – concerns a large number of structural failures which, due to the abrupt nature of the phenomenon, may cause loss of lives and damage to infrastructure. Therefore, it is crucial to develop numerical methods, besides certain theoretical and experimental approaches, to predict the whole process of mechanical failure from the elastic phase, the damage initiation, the stable and unstable propagation of failure until the final rupture. This dissertation studies a continuum damage approach, by focusing on the development of a nonlocal model with enhanced performance and accuracy in the modeling of localized quasi-brittle damage.

Aalto-DD 127/2021

ISBN 978-952-64-0514-8 (printed)
ISBN 978-952-64-0515-5 (pdf)
ISSN 1799-4934 (printed)
ISSN 1799-4942 (pdf)

Aalto University
School of Engineering
Department of Civil Engineering
www.aalto.fi